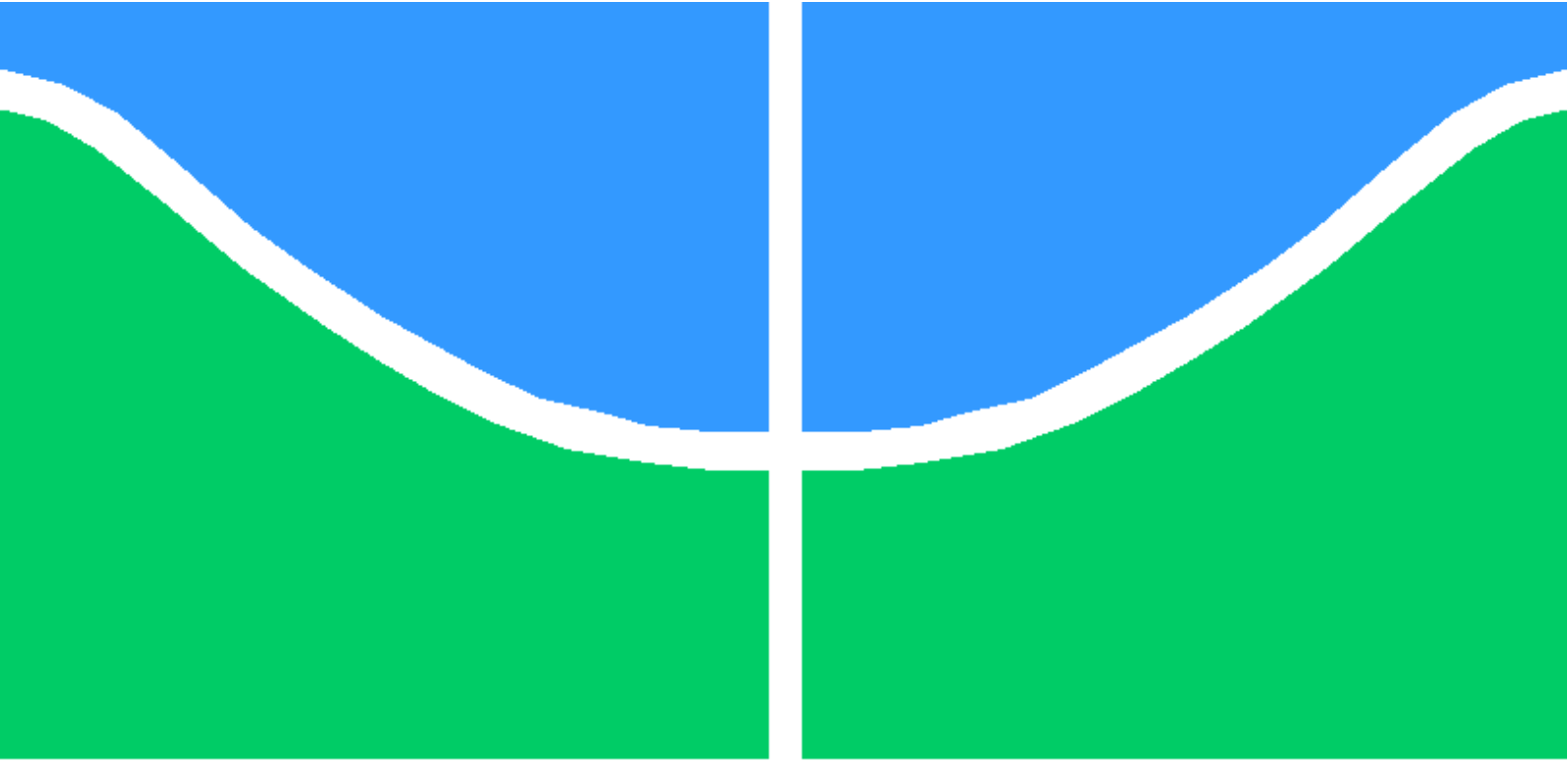

TRABALHO DE CONCLUSÃO DE CURSO

MIMO SAR: A technique for achieving full polarimetric, high resolution wide swath SAR

Bruno Pessoa Chaves

Brasília, Dezembro de 2019

UNIVERSIDADE DE BRASÍLIA

FACULDADE DE TECNOLOGIA

UNIVERSIDADE DE BRASÍLIA
Faculdade de Tecnologia

TRABALHO DE CONCLUSÃO DE CURSO

MIMO SAR: A technique for achieving full polarimetric, high resolution wide swath SAR

Bruno Pessoa Chaves

Relatório submetido ao Departamento de Engenharia Elétrica como requisito parcial para obtenção do grau de Engenheiro Eletricista

Banca Examinadora

Prof. Sébastien R.M.J. Rondineau, FGA/UnB _____
Orientador

Prof. Adoniran Judson de Barros Braga, ENE/UnB _____
Examinador interno

Prof. Leonardo Aguayo, FGA/UnB _____
Examinador interno

Agradecimentos

Eu gostaria de agradecer profundamente a todos que me ajudaram durante esse TCC e durante o curso de graduação como um todo. Em particular, eu gostaria de agradecer meus professores, que compartilharam comigo grandes conhecimentos a respeito da engenharia elétrica e me fizeram perceber que, embora difícil, a profissão de engenheiro eletricista é de fato a minha vocação, e é algo que me traz grande realização pessoal.
Mas principalmente, gostaria de agradecer a minha familia e a todos os meus amigos. Meu tempo na graduação foi difícil, e foi preenchido por muito estresse e insegurança. Sem vocês e todo o maravilhoso apoio que me deram, eu nunca teria acreditado em mim tanto quanto acreditei, e nunca teria chegado tão longe quanto cheguei. Por isso, vocês tem a minha mais profunda gratidão.

Bruno Pessoa Chaves

ABSTRACT

Synthetic-aperture radar (SAR) has become one of the most important remote sensing techniques in the last few decades. It allows for day-night operation and is resilient to difficult weather conditions. However, classic SAR has considerable limitations. The first one is that it has a trade-off between size of imaged area and resolution, meaning we can't have a wide area with a high level of detail, which is a big problem for many applications. The second limitation is that, to obtain full polarimetric information, either the imaged area must decrease in size or there must be a deterioration in resolution. In some applications that necessitate polarimetric information, this is likewise quite an issue. To deal with these limitations of classic SAR, MIMO (multiple input multiple output) SAR is a new technique that utilizes array processing to extract angular information from the received echo and thus obtain both a high resolution and a wide imaged area, along with polarimetric information. In this work, the theory behind MIMO SAR is presented, along with simulations that demonstrate the advantages of using this system over the traditional techniques.

RESUMO

SAR (radar de abertura sintética, do inglês *synthetic aperture radar*) tem se tornado uma das técnicas de sensoriamento remoto mais importantes nas últimas décadas. A técnica SAR permite operação tanto no dia quanto à noite, além de ser resiliente a condições climáticas adversas. No entanto, técnicas clássicas de SAR apresentam limitações consideráveis. A primeira é que existe uma relação de compromisso entre tamanho da área imageada e resolução, de forma que não conseguimos uma grande área com um alto nível de detalhe, o que é um grande problema para várias aplicações. A segunda limitação é que, para obter informação polarimétrica completa, ou a área imageada diminui ou a resolução piora. Em certas aplicações em que se necessita de informação polarimétrica, isso se torna um problema. Para lidar com essas limitações de SAR clássico, MIMO (múltiplas entradas múltiplas saídas, do inglês *multiple input multiple output*) SAR é uma nova técnica que utiliza processamento de arranjo para extrair informação angular da onda recebida e consequentemente obter tanto uma resolução fina quanto uma grande área imageada, junto de informação polarimétrica. Nesse trabalho, a teoria atrás de MIMO SAR é apresentada, junto de simulações que demonstram as vantagens de se usar esse sistema sobre as técnicas clássicas.

Table of contents

List of Figures

List of tables

Acronyms

DBF	Digital Beamforming
DLR	German Aerospace Center
DoA	Direction of Arrival
GMTI	Ground Moving Target Indication
HRWS	High Resolution Wide Swath
IFP	Image Formation Processing
LCMV	Linear Constraint Minimum Variance
MIMO	Multiple Input Multiple Output
PRF	Pulse Repetition Frequency
PRI	Pulse Repetition Interval
RCS	Radar Cross Section
SAR	Synthetic-Aperture Radar
SIMO	Single Input Multiple Output
TDM	Time Division Multiplexing

Symbol List

Latin Symbols

P_r	Received power
P_t	Transmitted power
G	Antenna gain
A_e	Effective antenna area
R	Distance
$s_r(t)$	Received signal
$s_t(t)$	Transmitted signal
$h(t)$	Impulse response
$\mathcal{R}_s(t)$	Signal auto-correlation
$rect$	Rectangular window
T_p	Signal duration
f_c	Carrier frequency
B	Signal bandwidth
PRF	Pulse repetition frequency
$u_n(t)$	Received signal at pulse number n
$R_n(x, y)$	Distance from point (x, y) at pulse number n
$g_n(x, y)$	Normalized gain in the direction of (x, y) at pulse number n
c	Speed of light
$h_n(t)$	Impuse response at pulse number n
Δt	Resolution in time
ΔR	Resolution in range
R_0	Range to the center of the scene at the middle of the aperture
V	Speed
x_a	Scene x coordinate
y_a	Scene y coordinate
y_{pl}	Platform y coordinate
z_{pl}	Platform height
Δx	Azimuth resolution
K	Factor to model system imperfections
L	Aperture length
W_s	Scene range swath

Z	Scattering matrix
$h_{np'p}(t)$	Impulse response of transmitted polarization p to received polarization p' at pulse number n
$h_{n,m}(t)$	Impulse response at antenna m at pulse number n
$y_n(t)$	Received signal at pulse number n
$a_{n,m}(t)$	Steering vector at pulse number n and time t
$\mathbf{r_m}$	Antenna position relative to phase center
$\hat{\mathbf{u}}$	Unitary direction vector
$\hat{\mathbf{z}}$	Unitary direction vector point at z direction
m	Antenna number
h	Platform height
M	Number of antennas
$\mathbf{w}$	Weight vector
w_m	Weight vector element at index m
$W(z)$	Z-transform of weight vector
$s_i(t)$	First transmitted signal
$s_j(t)$	Second transmitted signal
$s_p(t)$	Signal transmitted at polarization p
$R_n^m(x,y)$	Distance of point (x,y) to antenna m at pulse number n
$u_{np'}^m(t)$	Received signal of received polarization p' at antenna m at pulse number n

Greek Symbols

σ_a	Radar cross section
λ	Carrier wavelength
γ	Chirp rate
ϕ	Phase of received signal
α	Beam angle
$\zeta(x,y)$	Reflectivity at (x,y)
$\zeta_{p'p}$	Reflectivity of transmitted polarization p and received polarization p'
$\Omega(t)$	Set of pulses being received at the same time

Chapter 1

Introduction

1.1 Remote Sensing and Earth Observation

Remote sensing has become a very importation area in the past decades. It generally consists of airborne or spaceborne sensors that detect objects from a given scene and it is a vital tool in many Earth sciences, such as hydrology [1], ecology [2], meteorology [3], oceanography [4], glaciology [5] and geology [6]. It also has applications in military operations [7], intelligence [8], agriculture [9] and humanitarian applications [10]. All these applications depend on fine resolution, wide sensed area and low revisit times (meaning information is obtained regularly).

Remote sensing techniques can be separated into two classes. The first is passive remote sensing, where the sensor simply detects signals coming from the scene in a passive fashion, i.e. the sensing does not involve the transmission of any signals by the remote sensing platform. Passive remote sensing was the first kind to be developed and examples include optical imaging, multispectral imaging and hyperspectral imaging. These techniques have the benefit that they obtain a very large bandwidth of the imaging scene, which is vital for some kinds of analysis [11] [12].

The second type of remote sensing is active remote sensing, in which the platform transmits a signal and obtains information by receiving the reflected signal. The main technique of this kind is synthetic aperture radar (SAR). These techniques generally obtain the reflectivity of the scene, instead of properties like color (see Fig. 1.1). While these techniques have the disadvantage that they obtain a smaller bandwidth from the scene, they have a major advantage in that they can obtain images even at night and in difficult weather conditions [13]. In particular, SAR techniques are specially suited to regions like the Amazon, for example, that have a season of heavy rain [14].

Given these benefits, SAR has become a well-established tool for obtaining Earth data. Systems like TerraSAR-X [15], Sentinel-1 [16] and Radarsat-1 [17] have provided rich data which allowed for a myriad of studies on a wide range of subjects. Additional features of SAR systems such as ground moving target indication (GMTI) and Interferometric SAR have only intensified the utilization of SAR.

In the last few years, however, a few limitations of SAR have become apparent. As we will see in

Figure 1.1: Optical and SAR images of the same scene. We can see that the interpretation of the image is a bit more nuanced in the SAR case than in the optical case, since SAR obtains the reflectivity of the scene, instead of properties like color. Image taken from [23].

chapter 2, classic SAR techniques present a trade-off in terms of size of imaged area and resolution (resolution being defined as the amount of detail in an image). In situations where both fine resolution and a wide imaged area are important (for example, in the study of deforestation), this becomes a problem. Furthermore, quad-polarization systems present either a coarser resolution or map a smaller area than mono-polarization systems [18], which can also become a big problem since polarimetric data can be vital for some types of analysis [19] [20] [21] [22].

In the hopes of overcoming this limitations, a new type of SAR system is emerging. Digital beamforming SAR (DBF SAR) is a new technique that utilizes an antenna array to obtain angular information from the received echo (such as in Fig. 1.2) and, with it, surpass the trade-off between resolution and size of imaged area of classic SAR. This technique is the basis for the new Tandem-L system, which is being developed by the German Aerospace Center (DLR) and promises performance orders of magnitude better than current systems. However, the Tandem-L system will still suffer from coarser resolution or smaller imaged area in polarimetric SAR [24], and so another system being developed in the literature is the MIMO (multiple input multiple output) SAR system. This system transmits several orthogonal waveforms so as to obtain polarimetric systems without compromising the other aspects of the image. The theory behind MIMO SAR is still fresh, and therefore a full polarimetric MIMO SAR system may still be years off. However, it could provide major benefits even when comparing it to DBF SAR.

In this work, we will present both the theory behind MIMO SAR and a few simulations exposing its performance. In chapter 2 we will present the basic theory of classic radar and SAR, along with is limitations, in chapter 3 we will present the theory and the techniques used in MIMO SAR, in chapter 4 we will present the MIMO SAR simulations, and in chapter 5 we will conclude our work.

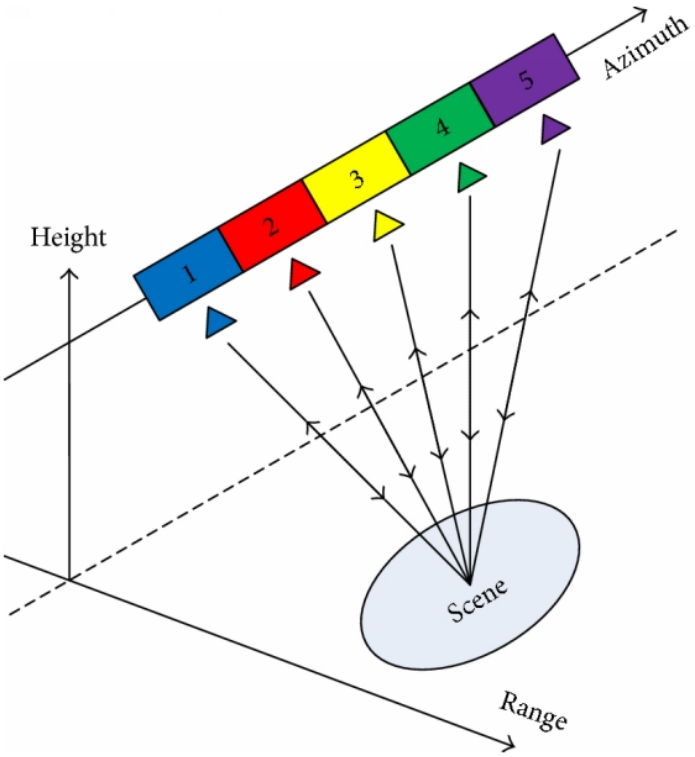

Figure 1.2: DBF SAR system, in which the SAR platform is equipped with an antenna array that is able to obtain angular information from the received echo, and thus overcome the trade-off between high resolution and size of imaged area present in classical SAR systems.

Chapter 2

Radar and SAR

2.1 Introduction

Before delving into MIMO SAR, we must first start with basic radar and SAR theory. From the classic theory, we shall see the limitations of the traditional systems that MIMO SAR seeks to overcome. In this chapter, we shall present the basic theory of radar and SAR. Naturally, the theory presented here is intended simply as an introduction into the topic. However, some useful intuition may be gained by analyzing the basic radar and SAR theory, even if briefly.

2.2 Radar

2.2.1 General Concepts

SAR theory starts with the theory of classic radar. The classic radar technique, whose name means 'radio detection and ranging' is the technique of transmitting a radio wave and, based on the wave reflected by the target, obtain characteristics from the target such as distance, size and reflectivity.

Fig. 2.1 shows the situation in classic radar. The antenna transmits a wave that reaches an object and is reflected back to the transmitting antenna. By measuring the time difference from the transmission to the reflection, one can measure the distance (also called range) between the reflecting object and the antenna.

The object itself is characterized by its radar cross section (RCS). The RCS of an object is a quantity that describes the power reflected by the target divided by the power density (measured in W/m^2) incident on it. The RCS is measured in squared meters and is equal to the cross section of a perfectly conductive sphere the would reflect the same power. More conductive materials reflect more power, and therefore metals have a greater RCS than other materials. Besides that, bigger objects naturally reflect more power, and consequently they possess a higher RCS. In this fashion, the RCS of an object contains information both about the size and about the material of an object,

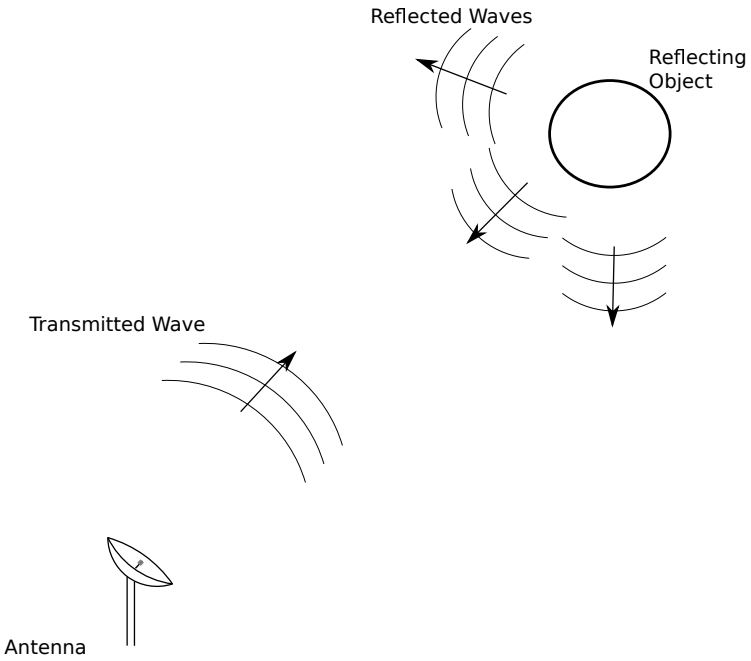

Figure 2.1: Situation considered in classic radar. The antenna transmits a wave and the target reflects it. The radar station then receives the reflected wave and performs signal processing on it so as to obtain useful pieces of information about the target.

and therefore it can be used to classify targets, which is widely used in military applications [25].

In summary, classic radar allows for a measurement both of distance (range) and of RCS of a target. Additionally, one can also obtain angular information through the technique shown in Fig. 2.2. A highly directive antenna is used and its beam is rotated. To perform the rotation, one can use both a physical rotation or array steering if one is using an array. For each angle, we obtain radar information about the targets being illuminated by the array. We can see that targets whose angular distances are smaller than the beamwidth cannot be separated, and therefore a high directivity (and hence a large antenna) is needed for a radar to obtain a good angular resolution. As we will see later, SAR is precisely a way to circumvent this angular resolution problem without the necessity of a large antenna.

2.2.2 Radar Equation

Another concept that is of major importance to properly understand radar techniques (and, later, SAR) is the radar equation. It related the power that is transmitted by the antenna to the power reflected by the way. For brevity, we will will not demonstrate this formula, but it can easily be proven using the Friis formula for free space radiation. The expression is:

$$P_r = \frac{P_t G \, \sigma_a A_e}{(4\pi R^2)^2}, \tag{2.1}$$

where P_r is the receive power, P_t is the transmitted power, G is the gain of the antenna, σ_a is the

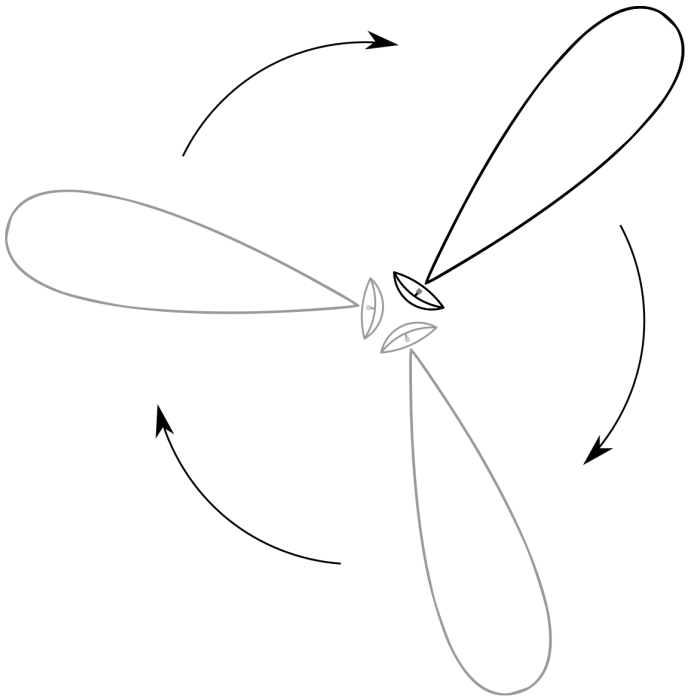

Figure 2.2: Top-down view of a radar system. The antenna is rotated to obtain angular information. For each angle, the system obtains radar information (RCS and range) for the targets illuminated by the antenna. As we can see, a highly directive antenna is needed for fine angular resolution.

RCS of the object, A_e is the effective area of the antenna (we remember that $A_e = \lambda G/4\pi$, where λ is the wavelength) and R is the range to the target. In eq. (2.1) it is important to notice that we consider a target that reflects the incident wave in an isotropic fashion (in other words, the wave is reflected with the same power in all directions).

Eq. (2.1) is of great importance to radar and to SAR since it relates the main quantities in radar and consequently is used to size the system. For examples, given a noise floor (which gives us a minimum acceptable value for P_r), we obtain a maximum detectable range, considering a fixed RCS. We can increase the transmitted power of the antenna area until we increase this distance to a desired value. Further down below, we will also see a more sophisticated version of this equation that is at the heart of the principle of operation of SAR systems.

2.2.3 Transmitted Signal and Matched Filter

Having considered the main system parameters and the working principle of classic radar systems, it is important to consider the transmitted waveform. To choose an appropriate waveform, we consider two objects whose distance difference to the radar platform is small. For example, the first target could be at range R_0 and the second could be at distance $R_0 + \Delta R$. The returns from the objects arrive at moments t_0 and $t_0 + \Delta t$. We have that the system must be able to separate these two returns.

To achieve this objective, one could think of transmitting a very brief pulse, i.e. with a short

duration, so as to be able to separate these very close targets. This was the first solution in radar [13]. This technique works, but presents a major problem: as the signal has a short duration and the energy of the signal must be high so that the return can overcome the noise, the transmitted power must be very high. A high power was difficult to be obtained with the electronics of the time, and therefore the achievable power was a limiting factor in obtaining a fine resolution [13].

However, it turns out that a fine resolution can be realized in an alternative fashion: a waveform of long duration could be transmitted and, in reception, a correlation could be performed between the received signal and the transmitted one. As a correlation with the transmitted signal is equivalent to a matched filter, a filter of this kind could be used to obtain a high temporal resolution even with a long duration signal. The resolution, then, is not limited by the power anymore, and the limiting factor becomes the transmitted bandwidth. To see this, we start with eq. (2.2):

$$s_r(t) = s_t(t) * h(t), \tag{2.2}$$

where $s_r(t)$ is the received signal, $s_t(t)$ is the transmitted signal and $h(t)$ is the impulse response of the scene. Once the impulse response of the signal is obtained, we obtain the RCS and the distance of each target, which is the desired information. We then apply a matched filter in eq. (2.2) to obtain:

$$\begin{aligned}
s_r(t) * s_t(-t) &= (s_t(t) * h(t)) * s_t(-t), \\
s_r(t) * s_t(-t) &= \left[\int s_t(\tau)h(t-\tau)d\tau\right] * s_t(-t), \\
s_r(t) * s_t(-t) &= \int \left[\int s_t(\tau)h(\lambda-\tau)d\tau\right] s_t(\lambda-t)d\lambda, \\
s_r(t) * s_t(-t) &= \int\int s_t(\tau)h(\lambda-\tau)s_t(\lambda-t)d\tau d\lambda.
\end{aligned} \tag{2.3}$$

We then define $u = \lambda - \tau$ and then:

$$\begin{aligned}
s_r(t) * s_t(-t) &= \int\int s_t(\tau)h(u)s_t(u+\tau-t)d\tau du, \\
s_r(t) * s_t(-t) &= \int h(u)\int s_t(\tau)s_t(u+\tau-t)d\tau du, \\
s_r(t) * s_t(-t) &= \int h(u)\mathcal{R}_s(u-t)du,
\end{aligned} \tag{2.4}$$

where $\mathcal{R}_s(t)$ is the auto-correlation of s_t. We note that if s_t has an infinite bandwidth, we have that:

$$\begin{aligned}
s_r(t) * s_t(-t) &= \int h(u)\delta(u-t)du, \\
s_r(t) * s_t(-t) &= h(t),
\end{aligned} \tag{2.5}$$

where $\delta(t)$ is the Dirac delta. Naturally, the bandwidth of the signal will never be infinite, however (as we will explore further in section 2.3.3) the time duration of $\mathcal{R}_s(t)$ will be inversely proportional to the bandwidth of s_t [13], and therefore the time resolution of the radar system will improve as the bandwidth increases. This is the reason many radar and SAR systems have wave-forms with bandwidths in the tens or hundreds of megahertz [13].

As resolution is only affected by bandwidth, we can design waveforms that have a large bandwidth at the same time as they have a long duration, so as to keep the signal power low. The most common solution is the following wave-form:

$$s_t = C\cos\left(2\pi f_c t + \pi\gamma t^2\right)\text{rect}\left(\frac{t}{T_p}\right), \tag{2.6}$$

where C is a constant related to the transmitted energy, f_c is the center frequency (or carrier frequency) of the signal, γ is the so called chirp rate, *rect* is the unitary rectangular window (that is equal to 1 is its argument has an absolute value smaller than 0.5 and is 0 otherwise) and T_p is the signal duration.

The signal s_t is eq. (2.7) is called a chirp signal, and is widely used in radar and sonar applications. A very important characteristic of the chirp signal is that, to a good approximation, the bandwidth B of the chirp signal is $B = \gamma T_p$. Therefore, we can make the bandwidth equal to any desired value by merely altering γ.

One final note in this section is that, from now on, instead of working with the notation of eq. (2.7), we shall express our signals exclusively using the complex envelope, that proves to be a more compact and practical notation to perform the operations present in the other parts of this work. Therefore, we express the signal s_t as:

$$s_t = Ce^{j\pi\gamma t^2}\text{rect}\left(\frac{t}{T_p}\right), \tag{2.7}$$

where j is the imaginary unit. The time dependence $e^{+j2\pi f_c t}$ will be omitted on the rest of this work.

Given that we have showcased radar fundamentals, we are ready to delve into the classic theory of SAR.

2.3 SAR

2.3.1 Working Principle and Geometry

The concept of SAR imaging was born when Carl A. Wiley [13] realized that a radar platform that was in relative movement with respect to a target could obtain angular information utilizing the Doppler effect. The situation is shown in Fig. 2.3. The points **x** and **y** are equidistant to the

platform, e consequently their reflected waves arrive at the platform at the same time. However, point $\mathbf{x}$ is getting closer to the platform, while point $\mathbf{y}$ is moving away from it. Consequently, due to the Doppler effect, the signal due to target in point $\mathbf{x}$ will have a positive shift in frequency, while the target in point $\mathbf{y}$ will suffer a negative shift. This gives us a means of separation the contributions from both points and therefore obtain a two-dimensional image.

Image 2.4 shows curves of constant range (that form circles on the ground) and of constant Doppler frequency (that form hyperbolas on the ground [26]). As we can see, each point can be distinguished by these two coordinates. However, because these coordinates are dependent on the (time-varying) platform position, generally we map the scene in another fashion: utilizing the coordinates of range and azimuth. The azimuth coordinate of a point $\mathbf{x}$ is defined as the projection of the point in the line of ground track. Therefore, the platform at a given time instant will have the same azimuth coordinate to a point $\mathbf{x}$ when the line connecting the platform to point $\mathbf{x}$ is orthogonal to the ground track. Azimuth is also often called the along-track coordinate, since it point in the same direction of the ground-track. For targets in the same azimuth (and therefore along the same line), their distance to the SAR platform will be different, and consequently we consider range as being the second coordinate. It is important to notice that, in normal SAR operation conditions, the illuminated area is very distant from the platform, in a such a way that the curves of constant range become approximately constant, and the range coordinate becomes orthogonal to the ground track. Because of this, the range coordinate is also called the cross-track coordinate. Finally, there is the concept of ground range. It is essentially the projection of range onto the ground, and is equal to $Rcos(\theta)$, where R is the range and θ is the grazing angle: the angle that the propagation vector of the transmitted wave makes with the ground.

2.3.2 SAR received signal echo and signal processing

As we saw, the working principle of SAR depends of the Doppler effect occurring on targets with the same range. To detect and separate these targets, it is necessary to make various transmissions of the same waveform, and to see how the frequency shift (or, equivalently, phase) varies with time. Therefore, we make the distinction between the so called fast time and the so called slow time. Fast time is the time in the reception of a single pulse, while slow time is the number of the pulse in question. Fast time is continuous in nature (although will be made discrete to allow for signal processing) and will be indicated with the letter t, while the slow time is discrete by nature (since the pulse transmission occurs in discrete moments) and will be denoted with the letter n. The pulses are transmitted with frequency PRF (pulse repetition frequency) and therefore 1/PRF seconds will pass between a given pulse n and the following pulse $n+1$. It is important to notice that, in SAR imaging, an integration time is necessary to image generation. In this integration time, the platform will travel a given distance and N pulses will be aggregated to generate the image. As we will see, a high value for N is desirable to obtain high resolution.

The distinction between fast time and slow time usually is accompanied with one of the most useful approximations in SAR: the start-stop approximation. In this approximation, we consider that, for a given fixed slow time n, the distance between the platform and any given point does

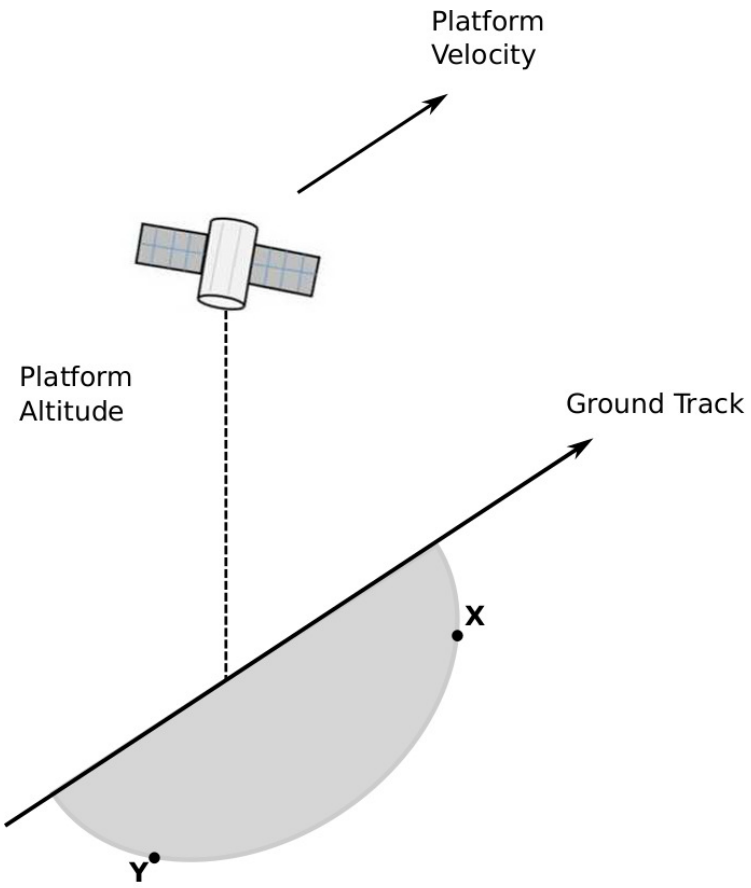

Figure 2.3: Situation considered in SAR. Note that points $\mathbf{x}$ and $\mathbf{y}$, even though they are at the same range, they have different Doppler frequencies since their movement relative to the platform is different. This difference in Doppler frequency gives us grounds to separate the contributions from these two points.

not change. In other others, we consider that the platform travels in discrete steps, and that it is fixed for fixed n.

Having defined the concepts above, we are now ready for the expression of the received signal. This expression has largely the same form of the radar equation and can be derived using the free space Green's function [27]. It is equal to:

$$u_n(t) = \int_A \frac{e^{-j2kR_n(x,y)}}{(4\pi R_n(x,y))^2} g_n^2(x,y)\zeta(x,y)\ s_n\left(t - \frac{2R_n(x,y)}{c}\right) dxdy, \tag{2.8}$$

where the integral is taken over the spatial domain A (which is the area being illuminated by the antenna beam), $s_n(t)$ is the n-th transmitted pulse, $u_n(t)$ is the signal received at instant t and considering pulse number n, and $R_n(x,y)$ is the distance between the platform to the point in (x,y) in slow time n. Note that $R_n(x,y)$ does not depend on t, which is the result of the start-stop approximation. Additionally, λ is the carrier wavelength, c is the speed of light and $g_n(x,y)$ is the antenna normalized gain. Generally, we consider that the platform antenna is highly directive, and

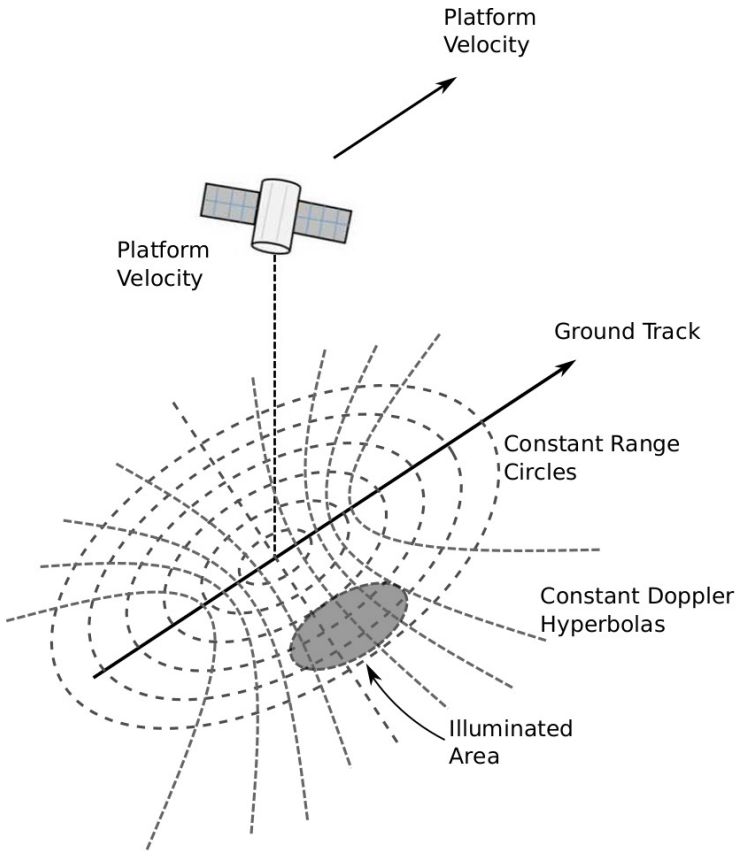

Figure 2.4: Curves of constant range (circles) and constant Doppler frequency (hyperbolas) in SAR operation.

consequently we can approximate $g_n(x, y)$ as being equal to one inside the beam and zero outside it, which simply limits the integration domain.

The main physical quantity to consider in eq. (2.8) is $\zeta(x, y)$. This quantity is the Fresnel reflection coefficient of point (x, y) and is the SAR analogue to the RCS of the scene, with three important differences: $\zeta(x, y)$ is a distributed quantity (over a given scene), while the RCS is concentrated and characterizes single objects (a single RCS number describes an aircraft, for example); $\zeta(x, y)$ relates the transmitted and reflected electrical fields, whereas RCS relates the power of the incoming and reflected waves; and, finally, $\zeta(x, y)$ is a complex number, i.e. it contains both magnitude and phase information. One can then see that one of the main differences between SAR and radar processing is that SAR operates with phase information, while this information is secondary in classic radar. We note that obtaining the SAR image equates to obtaining $\zeta(x, y)$.

In this manner, all SAR processing is performed so as to invert eq. (2.8) with respect to $\zeta(x, y)$. To this end, we first apply a matched filter (as descrived before) on signal $u_n(t)$. As the chirp signal has a large bandwidth, we have that the result is a good approximation for the impulse response of the scene. This impulse response is denoted by $h_n(t)$, since it depends on n, as illustrated in Fig. 2.5. The signal $h_n(t)$ is then passed through an image formation processing (IFP) algorithm. The IFP algorithm has the function of generation the final image based on $h_n(t)$, correcting for geometric distortions and platform imperfections.

Various IFP algorithms are used in SAR processing, such as the RDA algorithm [28], the Omega-K algorithm [29], the polar format algorithm [30] and the CSA [31], among others. The preference between one or the other stems mostly from the geometry of the situation and the achievable processing capacity. An in-depth description of IFP algorithms is outside the scope of this work, but it is crucial to emphasize one fact: all the IFP algorithms necessitate the knowledge of $h_n(t)$. As we will see below, guaranteeing the attainment of $h_n(t)$ imposes limits in classic SAR that motivate the research of MIMO SAR.

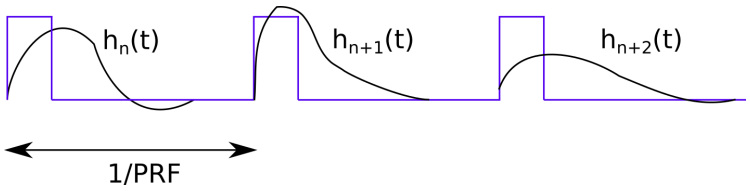

Figure 2.5: Signals in SAR. The blue waveform represents the transmitted signals, while the black waveforms are the impulse responses. The small differences between each impulse response allows for image formation. SAR imaging necessitates the attainment (and separation) of these impulse responses. This image represents three samples of slow time (three transmitted pulses) and an unspecified number of fast time samples.

2.3.3 Expressions for resolution and limits of classic SAR

Because of their huge importance to the comprehension of the limites of classic SAR techniques, we will now present the formulas for the resolution of SAR and the restrictions of the system parameters.

Firstly, we derive the range resolution. In an analogous fashion to classic radar, we have that in SAR the range resolution depends on our ability to distinguish returns from targets at different distances from the platform. As the fast time is clearly related to the distance (since the return time will always be $2R_n(x, y)/c$), we have that the resolution in range will be related to how well we can distinguish the impulse response in fast time t. As already established, a large bandwidth signal is necessary to achieve a thin autocorrelation function and therefore obtain a good replica of the impulse response. A good approximation [13] is to consider the width of the autocorrelation function to be:

$$\Delta t = \frac{1}{B}. \tag{2.9}$$

To relate this uncertainty in time to the uncertainty in range, we observe that the delay is equal to the distance times $2/c$, and therefore:

$$\Delta R = \frac{c}{2}\Delta t = \frac{c}{2B}. \tag{2.10}$$

The proof of the expression for the azimuth resolution is a bit more involved, and a complete derivation will not be shown in this text (for complete derivations, the reader is referred to [26] and [13]). However, a brief analysis still proves useful to understand the final expression and to develop some intuition. Firstly, we express the received signal due to a single point in coordinates $(x_a, y_a, 0)$, where the coordinate x_a is the azimuth (along-track) coordinate, y_a is the cross-track coordinate and the height of the target is considered to be zero. In the same way, the platform has coordinates $(n\frac{V}{\text{PRF}}, y_{pl}, z_{pl})$, in the same coordinate system. The parameter V is the platform velocity. We then have that the phase of the return signal (after the matched filter and ignoring the phase introduced by the scene reflectivity) is:

$$\begin{aligned}
\phi &= 2\frac{R}{\lambda} = 2\frac{\sqrt{\left(\frac{V}{\text{PRF}}n - x_a\right)^2 + (y_{pl} - y_a)^2 + (z_{pl})^2}}{\lambda}, \\
\phi &= 2\frac{\sqrt{\left(\frac{V}{\text{PRF}}n\right)^2 - 2\frac{V}{\text{PRF}}n\,x_a + R_0^2}}{\lambda}, \\
\phi &\approx 2\frac{R_0}{\lambda} - 2\frac{1}{R_0\lambda}\frac{V}{\text{PRF}}n\,x_a + \frac{1}{R_0\lambda}\left(\frac{V}{\text{PRF}}n\right)^2,
\end{aligned} \tag{2.11}$$

where R_0 is the distance from the platform to the target in $n = 0$. Often, $n = 0$ denotes the middle of the aperture, or the moment in which the platform has traveled half the total path. In the derivation of eq. (2.11), we considered that the distance between the point and the platform is much smaller than R_0. This hypothesis is not strictly necessary (and, in fact, various imaging algorithms do not use it [32]), but this approximation allows us to comprehend some characteristics of the SAR signal.

The phase derived in (2.11) represents a phase that varies with slow time n. As we can see, the phase is approximately a quadratic in n, and therefore it describes a chirp signal. The chirp rate is fixed by system parameters and by R_0. As before, we want to be able to separate various copies of this chirp signal (one for each point in the same range), and therefore we desire a large bandwidth for a non-ambiguous separation. As the chirp rate is fixed, we desire a long integration time to obtain a large bandwidth e consequently a high resolution. That is exactly what is being expressed in the formula derived in [26], that says that the azimuth resolution Δx is:

$$\Delta x = \frac{\lambda K R_0}{2L\sin(\alpha)} = \frac{\lambda K R_0 \text{PRF}}{2VN\sin(\alpha)}, \tag{2.12}$$

where K is a parameter do model system imperfections and α is the angle that the beam makes with the platform velocity (typically, $\alpha = \pi/2$ and the beam points broadside). The parameter L represents the aperture length: the length of the path traveled by the platform in the transmission of N pulses. As we can see, the resolution gets better the larger L is, e consequently it is of major importance in the design and in the use of SAR systems. We also see how this translated in pulse number: for a fixed PRF, we desire a large N to obtain a better resolution. The reason for that is clear based on the formula for the phase, derived in (2.11): the higher the chirp signal transmission,

the larger its bandwidth and therefore the better it can be distinguished from other chirp signals. Note that one peculiarity of SAR is that the expressions for the resolutions in the two dimensions are very different, which can often result in systems that have considerably different resolution values in each dimension.

Once we have expressed the formulas for the resolution, a question of major importance still remains: the fact that the possible values for the PRF are determined by the other parameters of the system. Firstly, we notice that there is an inferior limit for the PRF. This limit comes from the fact that the Doppler phase is perfectly described by its discrete samples in n only if the system PRF is high enough so that there is no aliasing. However, a large Doppler bandwidth is required for a fine resolution in azimuth. We can therefore prove ([13]) that:

$$\frac{V}{\Delta x} < \text{PRF}. \tag{2.13}$$

Additionally, there is also an upper bound on the PRF. To understand why, we consider a platform that illuminates a given scene. The antenna illuminates the scene such that the closest illuminated point is at distance R_1 and the farthest illuminated point is at distance R_2. The range swath W_s is then defined as the difference between the two, i.e. $W_s = R_2 - R_1$. An important observation is that, in reception, we must always be sure of what pulse is being received. In other words, we can't mistake the return of pulse n with the return of pulse $n+1$ and vice versa. To make sure of this, we cannot mistake an 'early' echo from pulse $n+1$ that reflected off the point with range R_1 from a 'late' echo from pulse n that reflected from the point with range R_2. This can also be seen in Fig. 2.5: if the PRF is too high, the different impulse responses will overlap, which will cause ambiguities. Since the time between two pulses is 1/PRF, we have that:

$$W_s < \frac{c}{2\text{PRF}}. \tag{2.14}$$

Taking into account both limits for the PRF, we have that:

$$W_s < \frac{c}{2\text{PRF}} < \frac{c}{2V}\Delta x. \tag{2.15}$$

The above equation is one of the most important in SAR. Since the PRF must always obey the above equation so that there is no ambiguities in range or azimuth, there exists a trade-off between a wide range swath (that, of course, is related to a wide imaged area) and a high resolution in azimuth. As we will see in chapter 3, this limitation of classic SAR is one of the main motivations for the creation of MIMO SAR.

2.3.4 SAR Modes

Having established the expressions for the resolution and PRF limits, we shall briefly show the main SAR modes of operation. The simplest one is called strip-map, in which the antenna beam

stays in a fixed angle. Since it is the simplest mode to be executed, it was also the earliest one to be developed.

There also exists the spotlight mode, in which the beam direction is continuously varied so as to always point in a fixed area. As we saw earlier, the azimuth resolution improves when the integration time increases, and consequently the spotlight mode presents the best azimuth resolution. An obvious disadvantage of the spotlight mode is its image has a much smaller area than strip-map or the third mode, ScanSAR.

In ScanSAR, the beam's direction is changed in time, following a zigzag pattern. The advantage of this mode is the wide imaged area. In fact, of the three main SAR modes, scan-SAR is the one with the widest imaged area, which of course comes with the worst resolution in azimuth. Therefore, this mode is useful when mapping a wide area is more important than having a good resolution.

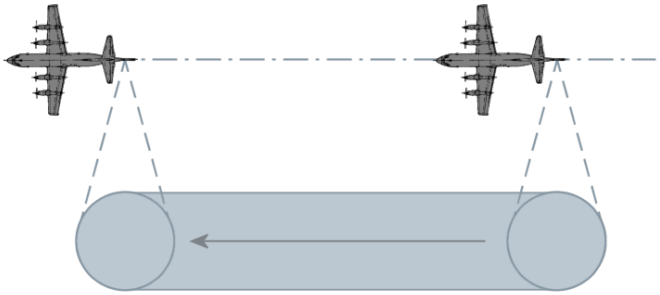

Figure 2.6: Stripmap mode SAR. The beam direction if fixed, and so the illuminated scene changes over time. This was the first mode to be developed.

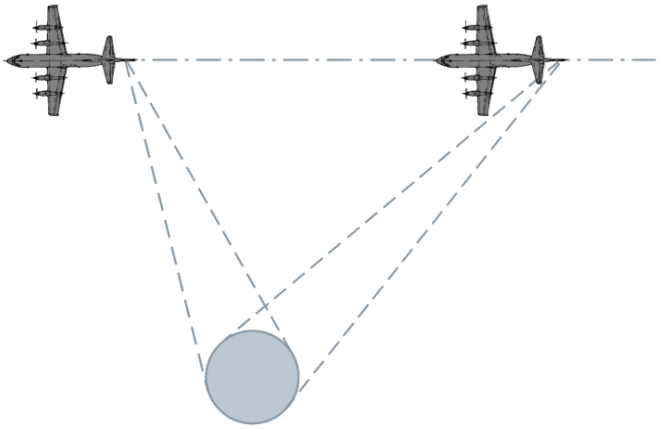

Figure 2.7: Spotlight SAR. The beam direction is changed so that the platform illuminated a constant area on the ground. Because the ingration time is longer, the azimuth resolution is better in this mode than in the others, at the cost of a much smaller imaged area.

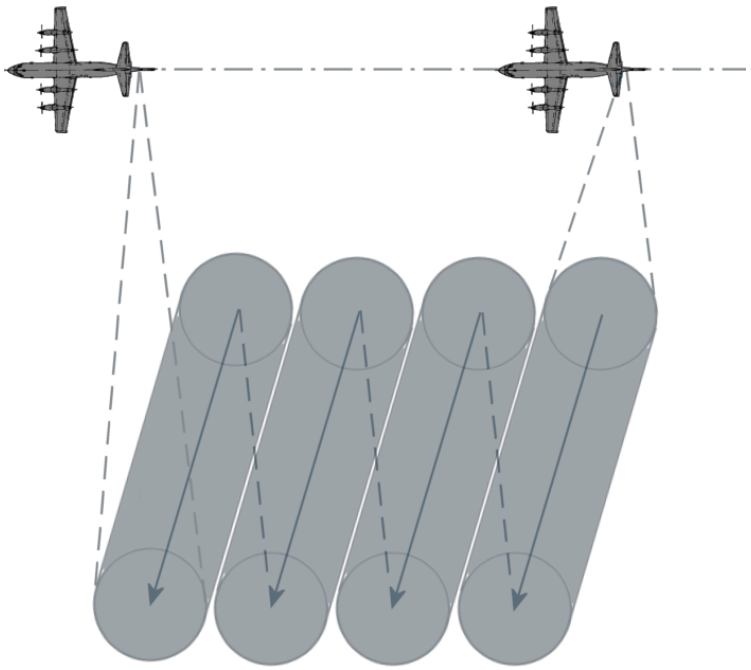

Figure 2.8: ScanSAR mode of operation. The illuminated changes in a zigzag pattern to obtain a wide image. As a consequence, the azimuth resolution is worse in this mode than in the others, since the integration time is smaller

2.3.5 Polarimetric SAR

One final point remains for understanding classic SAR techniques, and that is the issue of polarization. The polarization of an electromagnetic wave is defined as the orientation of the electric field in a plane wave. The discussion so far have treated with radar and SAR of a single polarization: a single polarization (for example, the horizontal one) was transmitted and the same polarization was received. However, a polarimetric data is considerably more useful for various remote sensing applications, such as forestry [19], military applications [20], agriculture [21] and topographic mapping [22], just to name a few. A full polarimetric SAR system has at least a pair of antennas, such that each one transmits and receives a different polarization.

The utility of polarimetric SAR comes from the fact that materials react differently to different incident polarizations. Additionally, materials can (and, in general, will) reflect polarizations which are different from the ones incident on them. For example, one can illuminate a target with a horizontal polarization and receive reflected signals in both the horizontal and vertical polarizations. Therefore, in a polarimetric context, the Fresnel reflection coefficient is substituted for the scattering matrix Z, in the following way:

$$Z = \begin{bmatrix} \zeta_{HH} & \zeta_{HV} \\ \zeta_{VH} & \zeta_{VV} \end{bmatrix}, \tag{2.16}$$

where the $\zeta_{p'p}$ coefficient is the Fresnel coefficient for the transmitted wave of polarization p and

reflected wave of polarization p'.

In the same way that the Fresnel reflection coefficient must be substituted by the scattering matrix, we also have to substitute the concept of impulse response by a matrix of impulse responses. In other words, the term $h_n(t)$ becomes $h_{np'p}(t)$, where we have an impulse response for each $p'p$ pair. Consequently, we must develop a system that is capable of obtaining $h_{p'p}(t)$ so that we can arrive at the polarimetric reflectivities.

Therefore, we must guarantee the separability of the received echoes in four distinct signals, one for each $p'p$ pair. As we already receive two antennas on reception that can distinguish between the two received polarizations, the difficulty is in separating the signals from the two transmitted polarizations. In other words, we have difficulty in distinguishing between the terms $h_{nHV}(t)$ and $h_{nHH}(t)$ or between the terms $h_{nVV}(t)$ and $h_{nVH}(t)$, but not betwen the terms $h_{nHH}(t)$ and $h_{nVH}(t)$.

To distinguish between the two transmitted polarizations, one has to make them orthogonal in some way. A first method could be transmitting wave-forms in two different bandwidths, one for each transmitted polarization. Therefore, the returns would be orthogonal regardless of the scene. The problem with this approach is that if the SAR system has a bandwidth B, each polarization will have access only to $B/2$ and consequently, as we saw, the resolution in range will worsen.

The most common solution is to separate the polarizations in time: the transmission are interleaved, such that each polarization is transmitted with half the PRF (similarly to a TDM system in telecommunications). The problem with this solution, however, is that a lower PRF naturally results in a worse resolution in azimuth (since we have to decrease the integration time to avoid aliasing). The PRF is then generally doubled so that a reasonable PRF in each polarization can still be achieved but, again, doubling the PRF has the cost of halving the range swath. This solution, even though it has its problems, is still the most used, and the trade-off imposed by it is seen as a price for having polarimetric information.

Obtaining a full polarimetric SAR system without decreasing the PRF, the range swath or the system bandwidth is one the main motivations for MIMO SAR, as we will see in the next chapter.

2.4 Conclusion

In this chapter, we reviewed the main features and limitations of radar and SAR systems. Developments in these systems have brought many advancements in many areas [33] [34] but, as we saw, important restrictions still limit the working of these systems. In the next chapter, we will see how MIMO SAR systems can overcome some of these restrictions and how they can bring great advancements for the area of remote sensing.

Chapter 3

MIMO SAR Theory

3.1 Introduction

As we saw on the last chapter, conventional SAR presents two severe limitations. The first one is that there is a conflicting requirement on the PRF: to obtain a fine resolution in azimuth, one needs a high PRF, but to achieve a large range swath, a low PRF is needed. Therefore, a fine resolution in azimuth is incompatible with a large range swath. In applications where you need both (such as deforestation monitoring), this presents a considerable limitation of SAR systems. The second limitation is that, to achieve full polarimetric SAR, either the signal bandwidth is decreased (which worsens the range resolution) or the PRF is lowered (which causes an inferior resolution in azimuth). We would, of course, like full resolution and full swath in full polarimetric SAR, but that is impossible with conventional SAR [18].

The solution to these limitations is MIMO SAR. The principle is implementing an array in the SAR platform where the received signal from each antenna is digitized individually. By then applying array processing on the signals, one is able to separate the waveforms both in terms of pulse number and in terms of transmitted polarization. In this chapter, we will mainly present one such MIMO SAR system showcases by the DLR [35]. In section 3.2, we will present the basic operation principle in the MIMO SAR system considered, in section 3.3 we will show how the system achieves a quad-polarimetric system, and in section 3.4 we will present a few other MIMO SAR systems.

3.2 Digital Beamforming for Pulse Number Selection

As we saw on the last chapter, one of the main limitations of classic SAR is the inherent trade off between swath width and azimuth resolution. This is because a a low PRF is required for the former, while a high PRF is needed for the latter. MIMO SAR circumvents this issue by utilizing array processing. In this sense, MIMO SAR allows for high resolution wide swath (HRWS) SAR.

The situation considered is illustrated in Fig. 3.1. We first choose a high PRF which is com-

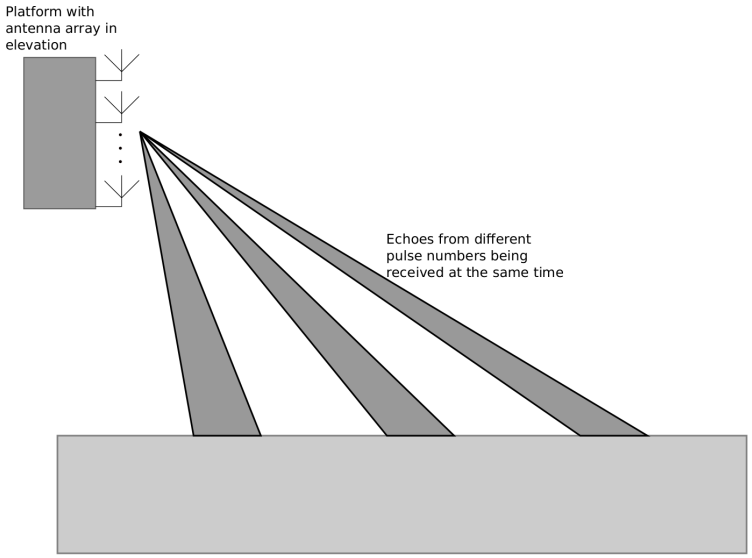

Figure 3.1: Operation principle of the considered MIMO SAR system. The platform is equipped with an antenna array in elevation, which is capable of separating the different echoes from the scene.

patible with the desired azimuth resolution. The platform transmits a signal at this PRF and, consequently, at any instant of time the platform is receiving echoes from different pulse numbers, which arrive at different angles. The platform is equipped with an antenna array. One very important characteristic is that the signal from each antenna is down converted and A/D converted individually (Fig. 3.2), so we have access to the individual signal received from each antenna. The received signals are:

$$s_m(t) = \sum_{n \in \Omega(t)} y_n(t) = \sum_{n \in \Omega(t)} (h_{n,m} * s_n)(t). \tag{3.1}$$

In this equation, n is the pulse number, $\Omega(t)$ represents the set of pulses arriving at the same

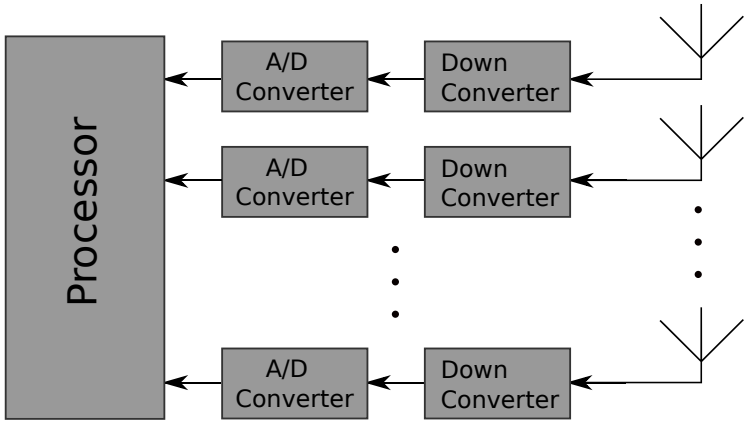

Figure 3.2: Architecture of MIMO SAR: each antenna array has its signal individually down converted and then sampled. In this fashion, we can perform beam forming in the digital domain.

time (note that both $\Omega(t)$ and its size are time varying), y_n is the return signal of pulse number n and it's equal to the transmitted signal times the impulse response $h_{n,m}$. Note that the impulse response not only depends on slow time but also on antenna number.

To achieve SAR imaging, we need the impulse response $h_n(t)$ and so processing on Eq. (3.1) must be performed. Note the difference between $h_n(t)$ and $h_{n,m}(t)$: the former does not depend on the receiving antenna, while the latter does. Indeed, $h_n(t)$ can be regarded as the impulse response on the phase center of the array (in this work, we will consider the phase center of the array as being the geometric center of array). This reasoning leads us to the following relation:

$$h_{n,m}(t) = h_n(t)a_{n,m}(t), \tag{3.2}$$

where $a_{n,m}(t)$ is called the steering vector [27]. It describes how the signal's direction of arrival (DoA) affects the phase at each antenna. We have that:

$$a_{n,m}(t) = e^{j\frac{2\pi}{\lambda}\mathbf{r_m}\cdot\hat{\mathbf{u}}(\theta(t),\phi(t))}, \tag{3.3}$$

where $\mathbf{r_m}$ is the position of antenna m relative to the phase center, the dot represents a scalar product, and $\hat{\mathbf{u}}(\theta,\phi)$ is the unitary vector pointing at the direction described by the (time-varying) angles θ and ϕ, which are respectively the spherical elevation and azimuth angles at the array. We see then that different angles produce different phase distributions along the array, in accordance to Eq. (3.3). This angle information gives a way to filter sources coming from distinct angles.

One important observation is that Eq. (3.2) is actually an approximation. It implicitly assumes that each echo is coming from a single angle. In fact, as illustrated in Fig. 3.1, each received echo occupies a small but not negligible region in angle space. As we will see in section 3.3, the fact that the echoes are distributed in angle space is essential for obtaining polarimetric information.

For the following discussion, we will again consider a coordinate system in which we have an x axis pointing at the along-track direction, a y axis representing the cross-track direction and a z axis pointing up. We also restrict our discussion to a linear array in which the antenna positions are distributed uniformly with a linear spacing of 0.5λ in the z direction such that:

$$\mathbf{r_m} = 0.5\lambda\, m\hat{\mathbf{z}}. \tag{3.4}$$

The spacing of 0.5λ was chosen because, in accordance to [27] and [36], it allows for unambiguous angle information with the minimum amount of antennas.

While our discussion will be restricted to a linear array, it will highlight principles that can be used for any type of array, as will be seen below. The expression for the steering vector becomes:

$$a_{n,m}(t) = e^{j\pi m\hat{\mathbf{z}}\cdot\hat{\mathbf{u}}(\theta(t),\phi(t))}. \tag{3.5}$$

Next, we derive an expression for the dot product in (3.5). We observe that the angle between $\hat{\mathbf{z}}$ and $\hat{\mathbf{u}}$ is simply θ. In other words, since the array is linear, the azimuth angle can be ignored since it does not influence the phase at each antenna. For a flat scene, it can easily be derived that:

$$\theta = \frac{\pi}{2} + \arcsin\left(\frac{h}{R}\right), \tag{3.6}$$

where h is the platform height with respect to the ground and R is the distance from a point in the scene to the platform. We also see that:

$$R = R_0 + \left(\frac{n_0 - n}{\text{PRF}}\right)\frac{c}{2}, \tag{3.7}$$

where R_0 is the range of some arbitrary reference pulse n_0 (remember that we are considering only a fixed time t, so each pulse number corresponds to a single range, under the approximation of Eq. (3.2)). We have therefore that:

$$a_{n,m}(t) = e^{-j\pi m \frac{h}{R_0 + \frac{n_0 - n}{\text{PRF}}\frac{c}{2}}}, \tag{3.8}$$

and hence:

$$s_m(t) = \sum_{n\in\Omega} y_n(t) = \sum_{n\in\Omega} (h_n * s_n)(t) e^{-j\pi m \frac{h}{R_0 + \frac{n_0 - n}{\text{PRF}}\frac{c}{2}}}. \tag{3.9}$$

Our objective is to apply signal processing in Eq. (3.9) so as to obtain $(h_n * s_n)(t)$ for all t. To achieve that goal, we can see that the signal $s_m(t)$ is a sum of harmonic functions in m. Each harmonic function has its frequency dictated by its angle, so that we can separate then if we apply a filter in the angle domain.

In references that discuss antenna arrays (such as [27]), this principle is illustrated further. First, we note that if we have M antennas, the combined signals form an M dimensional vector (for a fixed instant of time). To obtain the scalar $(h_n * s_n)(t)$, we perform a scalar product between the antenna signals and a vector $\mathbf{w}$, which contains weights to be applied to each signal. We then wish to find an expression for $\mathbf{w}$ such that:

$$(h_n * s_n)(t) = \mathbf{w} \cdot s_m(t) = \sum_{m=0}^{M-1} w_m s_m(t) \tag{3.10}$$

for all t.

As described in [27], we can take the Z-transform of $\mathbf{w}$:

$$W(z) = \sum_{m=0}^{M-1} w_m z^m. \tag{3.11}$$

This describes a polynomial in the z plane. Since this polynomial has M terms, it has $M-1$ zeros, and there we can choose $\mathbf{w}$ so as to place these zeros where they are needed. Recognizing that the signal $s_m(t)$ is mapped (through the Z-transform applied in the m dimension) to a set of points on the unit circle, where each point corresponds to a specific angle, we can then choose $\mathbf{w}$ as the coefficients of a polynomial in z which has zeros in the points corresponding to the points we want to suppress. If we perform this operation for each individual signal, we can separate all the desired signals. If we perform this operation for each t, we can separate the signals for all time. Fig. 3.3.

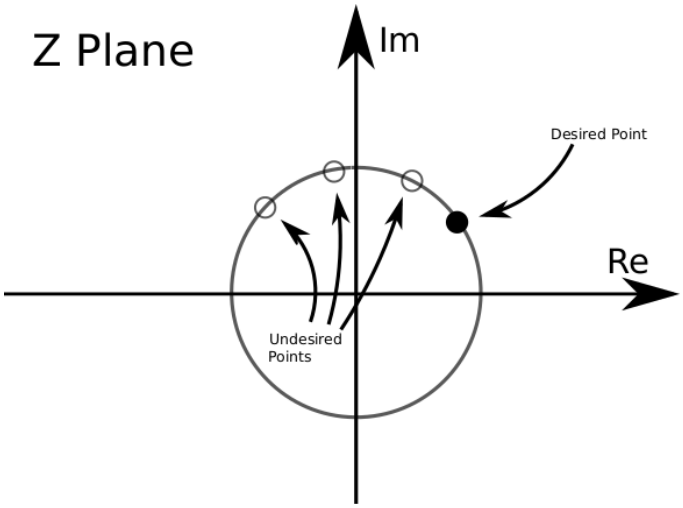

Figure 3.3: Separation of signals in the Z plane. Each signal is mapped into a different point in the unit circle. We then find the polynomial that is zero at the corresponding to the undesired signals, and obtain the corresponding weight vector whose elements correspond to the terms of this polynomial.

Having performed the operations above, we obtain $(h_n * s_n)(t)$. We can then perform matched filtering to obtain an estimate of $h_n(t)$, and can then continue with normal SAR processing. This technique of placing a zero response on each signal we want to suppress is called null-steering, and is widely used in MIMO communications (often under the name 'zero-forcing'). In communications, this technique allows for spatial multiplexing, and it fills a similar role in MIMO SAR: the separation of return signals, so as to map a wide swath while having a high PRF.

On a final note on this section, we note that using the described technique we can achieve a much wider range swath that what would be possible using classic SAR. In other words, we have a much wider swath for the same azimuth resolution, or the same range swath with a much higher resolution. The limitation on this system is then the capacity of the array to separate the different

echoes that return at the same time. This is both a function of array size and number of antennas [36], so one could say they are the limiting factor in MIMO SAR. We also have to take into account the extra processing and amount of data that are needed in MIMO SAR, which also could prove to be a very relevant limiting factor.

3.3 Polarimetry

The technique in the previous section allows us to tackle one big limitation of classic SAR, and allows for high resolution wide swath imaging. The other considerable limitation of classic SAR techniques described in chapter 2 is the problem of obtaining full polarimetric data while still having the full swath and full resolution. As we will explain in this section, this is also possible with MIMO SAR.

The basic idea when obtaining quad-polarization data is having two wave-forms that are separately transmitted in the two polarizations. These wave-forms must be designed so that they are separable once they are reflected back to the platform. We already presented two methods of doing so: having wave-forms which occupy different bandwidths and having wave-forms which are transmitted at different instants in time. As we saw, the problem with these solutions is that either the resolution significantly worsens or the range swath decreases by half. Therefore, solutions have been suggested in which we transmit two orthogonal wave-forms that occupy the same bandwidth and time interval.

The most common proposal of this kind is the one using up and down chirps. They are denoted by $s_i(t)$ and $s_j(t)$ respectively and given by:

$$s_i(t) = e^{j\pi\gamma t^2}\text{rect}\left(\frac{t}{T_p}\right) \tag{3.12}$$

and

$$s_j(t) = e^{-j\pi\gamma t^2}\text{rect}\left(\frac{t}{T_p}\right). \tag{3.13}$$

They are called up and down chirps since their frequency increases for the first and decreases for the second. It may be noted that the chirps occupy the same bandwidth and time interval, as desired. The chirps are orthogonal, in the sense that:

$$\int s_i^*(t)s_j(t)dt = 0. \tag{3.14}$$

This led some (for example [37] and [38]) to believe that, if these two wave-forms were to be transmitted, the echoes would, too, be orthogonal and hence we may separate the four polarizations. However, as shown in [18], this is not so. The reason for this is that Eq. (3.14) is not enough

for separability. Since the impulse response of the scene has a considerable time duration, the transmitted signals are 'stretched' in time, which means that the required condition is actually:

$$\int s_i^*(t)s_j(t+\tau)dt = 0, \quad \forall\tau \in \mathbb{R}. \tag{3.15}$$

The above expression is a cross-correlation between $s_i(t)$ and $s_j(t)$. Using the convolution theorem for the Fourier transform, one can easily see that the above equation is only obeyed if $s_i(t)$ and $s_j(t)$ do not have an overlapping bandwidth. As discussed in chapter 2, this is not acceptable, since it results in a worse resolution in range.

The compromise found in [18] is to use wave-forms that obey Eq. (3.15) only for a subset of values for τ, for example:

$$\int s_i^*(t)s_j(t+\tau)dt = 0, \quad \forall\tau \in \left(-\frac{\Delta\tau}{2}, \frac{\Delta\tau}{2}\right). \tag{3.16}$$

The reasoning for this compromise is that it is relatively simple to find wave-forms that obey the above equation and also because, as we saw in the last section, the time delay of an echo is dependent on the arriving angle of the returning wave. Therefore, in a manner similar to the one in the last section, we can separate waveforms that have a distinct DoA by using digital beamforming, while the separation for similar DoA's (which correspond to small time displacements) is taken care of by the above equation.

The wave-forms that obey Eq. (3.16) are called 'short-term shift-orthogonal wave-forms'. One such set of wave-forms is the one based on the classic chirp waveform. The first waveform, $s_i(t)$, is the classic chirp (for example the up-chirp), while the second, $s_j(t)$ is given by a chirp which has a discontinuity in phase, as shown in Fig. 3.4. The intuition behind these waveforms is that they are the signals with linear phase whose instantaneous frequency separation is maximized.

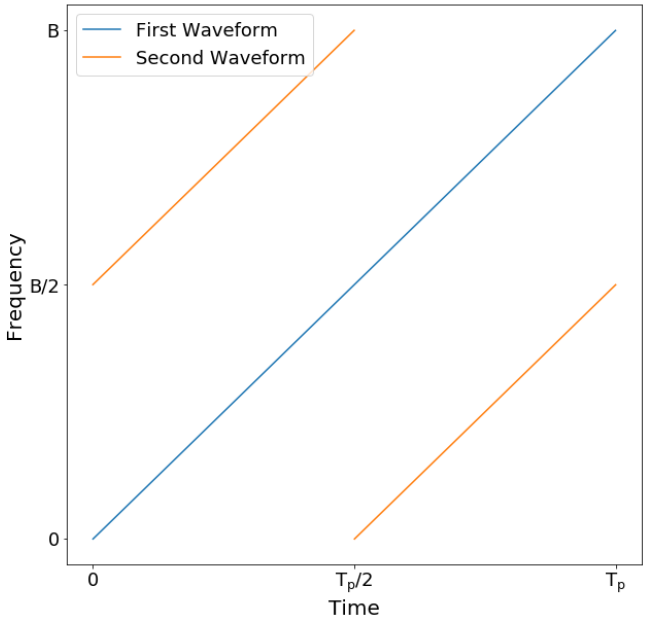

Figure 3.4: Instantaneous frequency of the signals transmitted in MIMO SAR. The first signal is the typical up-chirp, while the second is designed to be orthogonal to the up-chirp for small time displacements.

Another processing step that was proposed in [35] and [39] to achieve quad-polarization is the utilization of a filter bank before the digital beamforming. Figure 3.5 shows the overall architecture. The reasoning behind this filter bank is that at the output of each filter, the signals will have a separation in time. This separation in time improves the separation of the signals, since the response of $s_i(t)$ and $s_j(t)$ will be coming from different angles.

3.4 Other MIMO SAR systems

Besides the MIMO SAR system explained in the previous sections, there are a lot more systems that employ the same principle. We will briefly review them in this section. They are all taken from [40] and [41].

While in this work we will be focusing on arrays with multiple elevation beams (so as to separate the range echoes), it is also possible to consider arrays with multiple azimuth beams. In this configuration, the array antennas are placed in an along-track configuration. In this way, the platform receives echoes at several displaced positions, which effectively increases the PRF without diminishing the swath width. This technique is a SIMO (single input multiple output) technique, and is called strip-map SAR with multiple azimuth channels [41]. One downside of this technique is that it requires a substantially long antenna in the along-track direction.

One improvement that can me made in this regard is the transmission of two orthogonal wave-

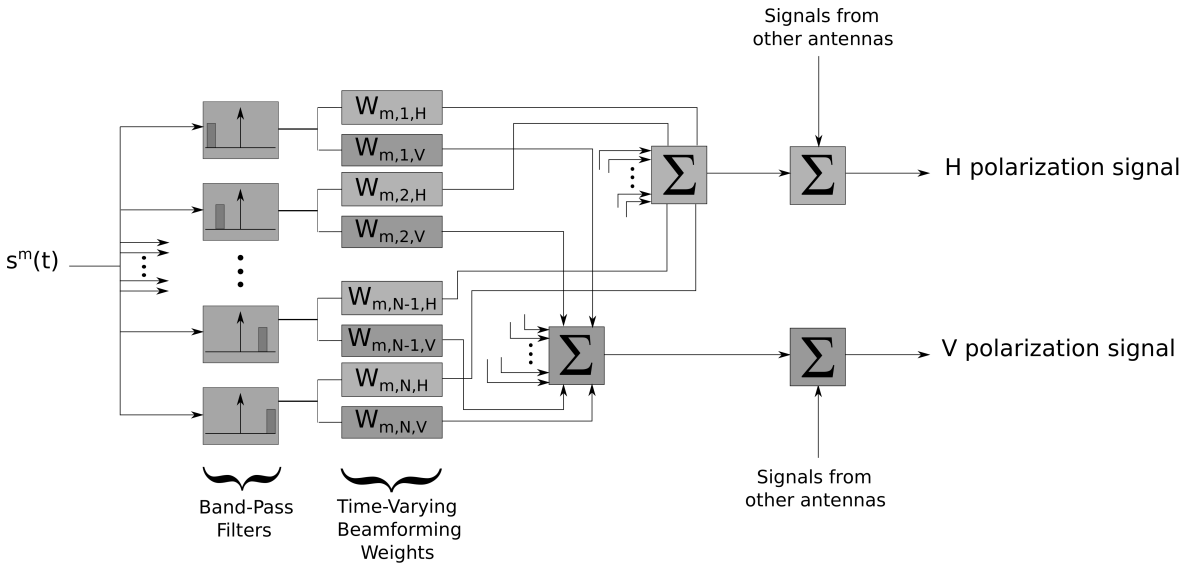

Figure 3.5: MIMO SAR processing. The signal first passes through a filter bank that displaces the signals from the two polarizations in time (and, consequently, also in angle). Digital beamforming then separates the signals from the two polarizations, as well as the signals with different pulse numbers n.

forms at the trailing and leading antennas of the array. The theory behind this technique is that each pair of transmitting and receiving antennas is equivalent to one transmitting and receiving antenna (called a phase center [42]) placed between the two, if a phase term is corrected [42]. Therefore, if two antennas are transmitting (and not just one, as previously), one obtains more phase centers and is consequently able to reduce the total numbers of antennas. Because of the two transmitting antennas and wave-forms, this is a MIMO technique and is called MIMO SAR with multiple azimuth channels.

Similar to the previous two, Scan-SAR with Multiple Azimuth Channels (also called TOPS [40]) employs azimuth channels together with a Scan-SAR operation (described in the last chapter) to map a wide area with a moderate antenna length. References [41] and [40] discuss a few problems present in this technique such as squint angle variations and how they create undesirable effects on the received signal.

The three modes described above are based on azimuth channels, which correspond to an along-track array. The main technique of this work, which was described on the last sections, is a part of another family of methods that utilize elevation channels. Other techniques of this family include systems that employ slow PRI (pulse repetition interval) variation and staggered SAR.

PRI variation methods are used for one simple reason: generally, spaceborne radars cannot transmit and receive at the same time. Therefore, there are blind ranges in which the platform does not receive any signal, and consequently no information can be derived about these regions. One solution to this problem is to slowly vary the PRI such that these blind ranges change from pulse to pulse, so that, over many pulses, we receive information from the whole illuminated scene. Staggered SAR works further on this concept, and allows for faster variations of the PRI to obtain

some nice properties, such as making sure that no two blind ranges are the same in two consecutive pulses. Staggered SAR was also chosen as the baseline for the DLR's new Tandem-L system, which promises to push SAR systems farther than ever before.

3.5 Conclusion

As we saw in this chapter, the use of arrays in which every received signal is digitized allows for SAR systems that fundamentally tackle the limitations present in classic SAR systems. Specifically, they allow for high resolution wide swath imaging, and also for quad-polarization imaging without deterioration neither in swath width nor in azimuth resolution.

We focused our attention to systems with an array in elevation. As we saw, there are many other MIMO and SIMO systems that can be used to achieve the imaging objectives. However, they all work with generally the same principle, and insight into any one specific system allows us to gain intuition on the others. Moreover, the staggered SAR system which was chosen as the baseline for the new Tandem-L system mainly works with an array in elevation, and so it may pay to study this one more thoroughly.

In the next chapter, we will present simulation results regarding the system presented in this chapter. We will consider the system as it performs spatial and frequency processing to separate the echoes in range and the signals from different polarizations. For simplicity, however, we will not deal with the issue of blind ranges. For simulation results regarding blind ranges and staggered SAR, the reader is referred to [43] [44].

Chapter 4

MIMO SAR Simulation

4.1 Introduction

In this chapter we will present simulation results of the MIMO SAR system described in the previous chapter. Our simulations are based on the RITSAR Python package [45], which implements the imaging formation algorithms.

4.2 Simulation Setup

4.2.1 Procedure

The first step in the simulation is acquiring the received signal according to a slightly modified version of Eq. (2.8). We first set up a scene consisting of a sequence of positions and a sequence of associated reflectivities. We then consider a list of platform positions that change with pulse number. In this simulation, we are employing the start-stop approximation, as described before.

The received signal in the MIMO SAR simulation differs from Eq. (2.8) in two ways. The first is that each antenna receives a slightly different phase depending on the antenna's position. Therefore, we also have a list of antenna positions in relation to the platform. From this information, we obtain the distance from each antenna to each point in the scene, which is the quantity $R_n^m(x, y)$.

The second is that we consider a quad-polarization system, and therefore the received signal depends on received polarization p', the transmitted signal depends on transmitted polarization p and the Fresnel reflection coefficient depends on the pair $p'p$. The equation then becomes:

$$u_{np'}^m(t) = \int_A \frac{e^{-j2kR_n^m(x,y)}}{\left(4\pi R_n^m(x,y)\right)^2} \zeta_{p'p}(x,y)\ s_p\left(t - \frac{2R_n(x,y)}{c}\right) dxdy. \tag{4.1}$$

The two signals s_p are the short-term shift-orthogonal waveforms described in section 3.3. We note that we will not be modeling antenna gain in this work, and will only be utilizing the common

approximation of considering a gain of one over an illuminated scene and zero outside it, with an abrupt change at the boundary of the scene.

The signal $u^m_{np'}(t)$ is then passed through FIR filters. The filters spam the bandwidth of the baseband signal, coincides with the sampling frequency in the simulation.

The final processing step is the spatial filtering. Many works utilize Linear Constraint Minimum Variance (LCMV) beamforming [35], which can be considered an 'optimal beamformer' [46], since it separates the signals while maximizing the signal-to-noise ratio. In this work, however, we will utilize the simple null steering described in chapter 3, because of its simplicity. Like in chapter 3, we consider vertical arrays, in which the antennas are displaced in elevation with a displacement of $\lambda/2$.

To obtain the received wave from the transmitted pulse with transmitted pulse n, we recognize that (in a situation with a high enough PRF) we will be receiving simultaneously multiple signal returns, each with coming from a different angle. In the null-steering technique, we simply weight the signals from each antenna so as to place a null on the undesirable signals. Likewise, we must separate the signals from the two different polarizations. To accomplish that, we notice that, in each filter, we will be receiving one signal at a given range and the other signal will be coming from a range that is shifted either forward or backward by a time delay of $T_p/2$. Therefore, we can place an additional zero at the angle of this unwanted signal, so as to receive the desired polarization. In short, if we are receiving $2N$ signals at the same time (N pulse numbers and two signals for each pulse number, each one respective to a different polarization), we apply $N+1$ weights, so as to have N zeros in the angle domain ($N-1$ zeros to filter the other pulses and 1 zero to filter the signal from the other polarization). Of course, we repeat this process for each of the $2N$ signals, and also for each filter, and so we see that the processing increases quite a bit when in comparison to traditional SAR.

After the beamforming, we apply the matched filter and continue with normal SAR processing. To generate the image, we utilize the polar format algorithm [26]. In the next section, we will show the results from our simulation.

4.2.2 Parameters Considered

We will consider the system parameters shown in table 4.1. We note that R_0 is the distance from the platform to the scene center at the middle of the aperture. These parameters were largely taken from the upcoming DLR's Tandem-L system[24]. Note that Tandem-L is not a realization of the MIMO SAR system described in the previous chapter: while it employs digital beamforming on receive to achieve HRWS SAR, it does not employ multiple waveforms to obtain polarimetric information. Nevertheless, we shall use it in this work as it represents realistic values for an L-band SAR platform.

For the scene, we chose a scene with a wide swath, so as to show the advantages of MIMO SAR. From equation (2.14), we have that $W_s < c/2\text{PRF}$. Since we have a PRF equal to 500 Hz, we have that the maximum value for W_s is equal to 300 km. We chose exactly this value as our swath.

Parameter	Value
Carrier Frequency f_c	1.26 GHz
Chirp Bandwidth B	200 MHz
Pulse duration T_p	15 μs
Sampling Frequency	200 MHz
PRF	500 Hz
Total number of pulses transmitted	975 pulses
Integration time	1.950 s
Platform altitude	750 km
R_0	1340 km
Speed	7.5 km/s
Number of antennas	4

Table 4.1: System parameters considered in the simulation.

From [24], we see that the farthest point in the illuminated scene from Tandem-L has an incident angle of 30° with respect to the platform. Using this same angle as indicating the farthest point in our scene, and using a little trigonometry, we arrive at the fact that our scene starts from angle 38.76°. The slant range of the closest point is 1190 km and the slant range of the farthest point is 1490 km. The ground ranges are 928 km and 1290 km, respectively (we recall that the ground range is the projection of the range onto the ground).

As for the simulated scene itself, we encounter a little bit of a conundrum: while we want a scene that occupies the whole swath so as to see the eventual benefits of MIMO SAR, we also want a small scene so that we can better appreciate the effects that various techniques have on resolution. Therefore, we reach a compromise: our scene consists of two very small regions. The first and second regions are located respectively at the closest and the farthest points in the illuminated region on the ground. The regions have an azimuth coordinate of zero. The images contained in the two regions (along with their coordinates) are shown in Figs. 4.1 and 4.2. The white points have reflectivity equal to one. This approach also has the benefit of being much easier to simulate, since we have fewer points that contribute to the received signal.

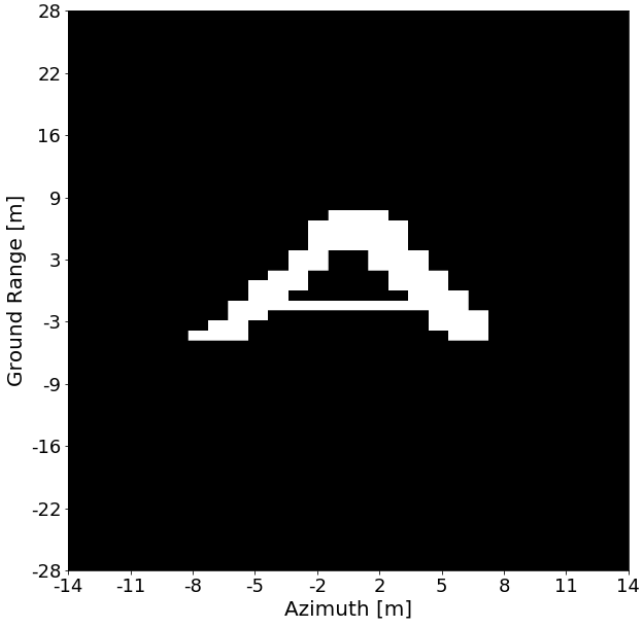

Figure 4.1: Image in the closest region of the illuminated swath.

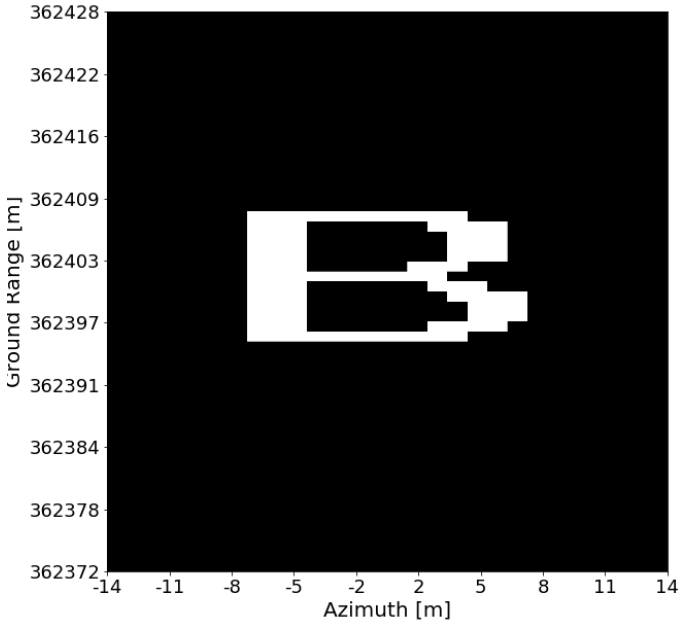

Figure 4.2: Image in the farthest region of the illuminated swath.

4.3 Simulation Results

4.3.1 Classic SAR

Before showing MIMO SAR results, it is useful to first show classic SAR processing applied to these images. Since the system (intentionally) obeys all SAR limits in terms of range swath, integration time and PRF, we do not have any azimuth or range ambiguities. We therefore consider just one antenna, one signal and simply perform the matched filtering followed by the IFP.

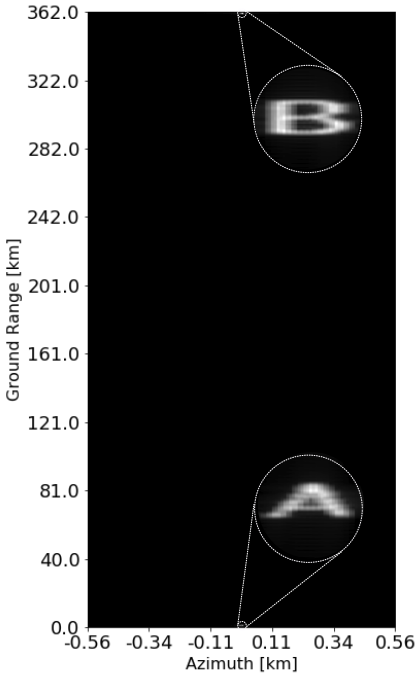

Figure 4.3: Full image generated from classic SAR processing on the whole scene.

Fig. 4.3 shows our results of the whole scene. The image regions are at the very top and at the very bottom of the image (with a zoomed in version to help visualization). Since the scene is very large in comparison to the small regions, it is very inconvenient to display our results like this, and therefore we shall display only the zoomed in versions from now on, such as in Figs. 4.4 and 4.5, that shown a 'zoomed in' version and display the regions of interest. The location of these images in the scene as a whole can be deduced from the labeled azimuth and range coordinates.

Figs. 4.4 and 4.5 show the images after SAR processing. The scale is linear, and shall be so for most of the remainder of the images in this chapter. As can be seen, the images provide a very good representation of the original scene, with only an expected blur, which results from the limited resolution in resolution and range.

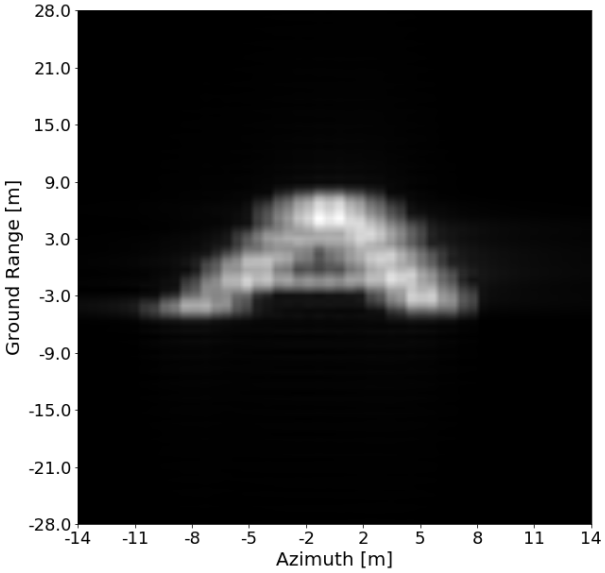

Figure 4.4: Image generated from classic SAR processing on the closest region in the scene. The PRF is 500 Hz, such that there is no range or azimuth ambiguity.

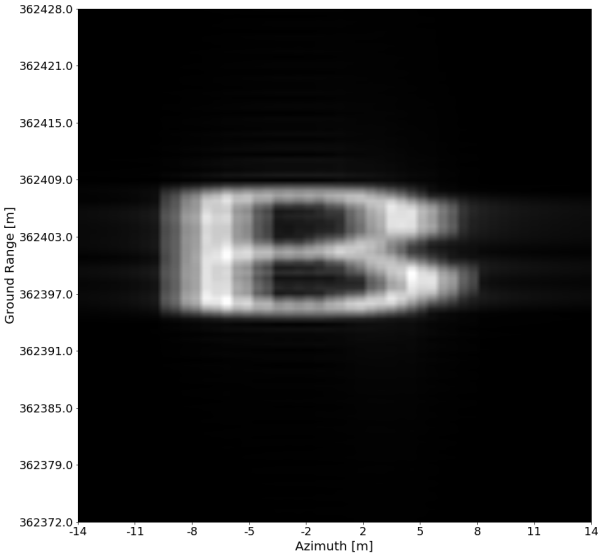

Figure 4.5: Image generated from classic SAR processing on the farthest region in the scene. The PRF is 500 Hz, such that there is no range or azimuth ambiguity.

Suppose, however, that for some application, the azimuth resolution in Figs. 4.4 and 4.5 is not enough: finer resolution is needed. We can then increase the integration time along with a proportional increase in the PRF so as to avoid azimuth ambiguities. To achieve this, we increase

both the integration time and the PRF threefold: the new integration time is 5.85 s and the new PRF is 1.5 kHz. Figs. 4.6 and 4.7 show the results. Analyzing the two images, the first thing that can be noticed is that the result is quite the opposite of the desired one: the resolution in azimuth is much worse than before. Another important observation is that the range coordinate is significantly off - by tens of kilometers, in fact. Of course, these results stem from the fact that the swath is wider than what is allowed in classic SAR for the PRF of 1.5 kHz.

The azimuth resolution deterioration (which in consistent with the literature [47]) is most likely because of range cell migration. A explanation of range cell migration is a bit involved an is outside the scope of this work (for a detailed explanation, see [13]) but it is essentially a geometric distortion that needs to be compensated by the IFP. If a return appears in the wrong range bin (as is the case), the algorithm can compensate in the wrong way and this, along with the distortion itself, causes a deterioration of resolution. The other effect, of the range coordinate being displaced from its true value, has a more direct explanation: since the returns are periodic, the platform cannot distinguish between returns from a given target with distance R from the returns of the target with distance $R + c/2\text{PRF}$, and from this ambiguity the range coordinate is displaced.

Having shown the limitations of classic SAR for a situation of HRWS imaging, in the next subsections we present simulations of the MIMO SAR system.

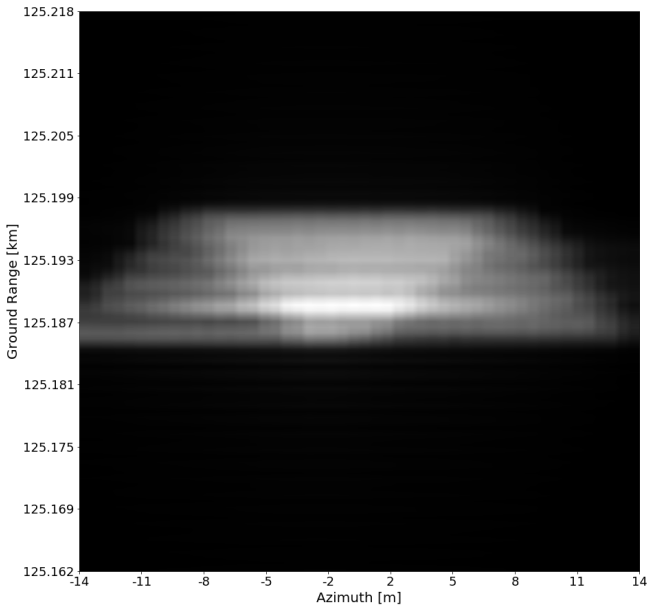

Figure 4.6: Image generated from classic SAR processing on the closest region in the scene. The PRF is 1.5 kHz, such that we have range ambiguity in this case. This results in a huge image deterioration in range, along with a shift in range position.

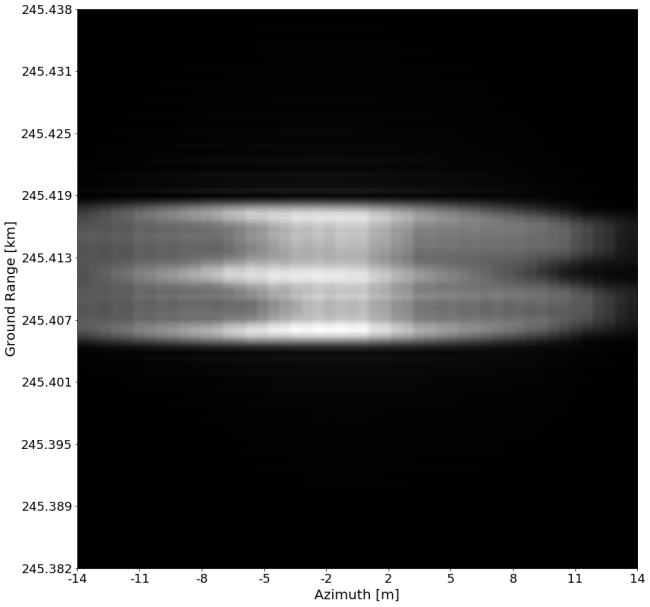

Figure 4.7: Image generated from classic SAR processing on the farthest region in the scene. The PRF is 1.5 kHz, such that we have range ambiguity in this case. This results in a huge image deterioration in range, along with a shift in range position.

4.3.2 Filters

As shown in chapter 3, the first step in MIMO SAR processing is filtering. For this simulation, we considered 6 filters that each cover a section of the signal bandwidth. Each filter has 42 taps and is arrived at by the window method, utilizing a Hamming window. Fig. 4.8 shows the magnitude response of each filter. Note that each one covers a section of the full bandwidth. Also note while it may appear that some frequencies have a smaller gain than others, Fig. 4.9 shows us otherwise. This graph shows the magnitude response of the sum of all the filters. As we can see, is is equal to unity for all frequencies. Likewise, the phase response of the sum of the filters is linear, with a group delay of only 97 ns. These two features (unitary gain on all frequencies and linear phase with small group delay) are important because the filter bank is meant only to separate the two MIMO SAR signals, and not to cause any type of distortion. Indeed, the ultimate goal is to sum the outputs of all the filters, so ideally they shouldn't introduce any distortion.

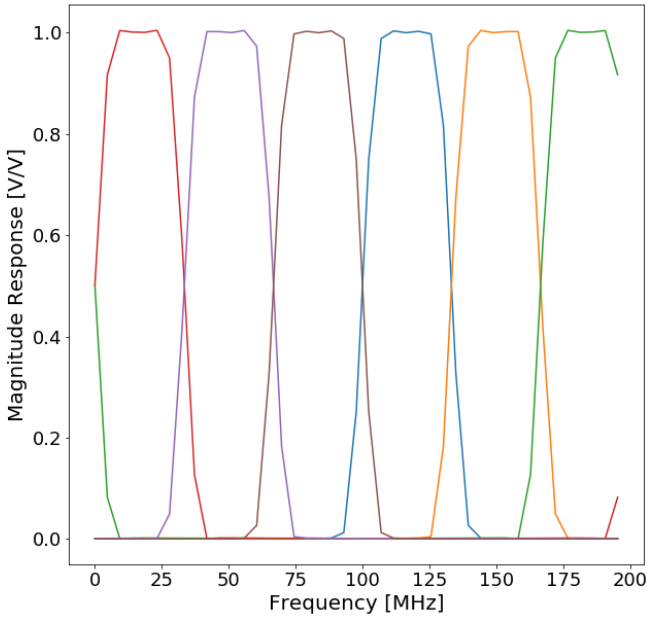

Figure 4.8: Magnitude responses of the 6 filters used in the MIMO SAR processing. Each filter covers a subsection of the signal bandwidth.

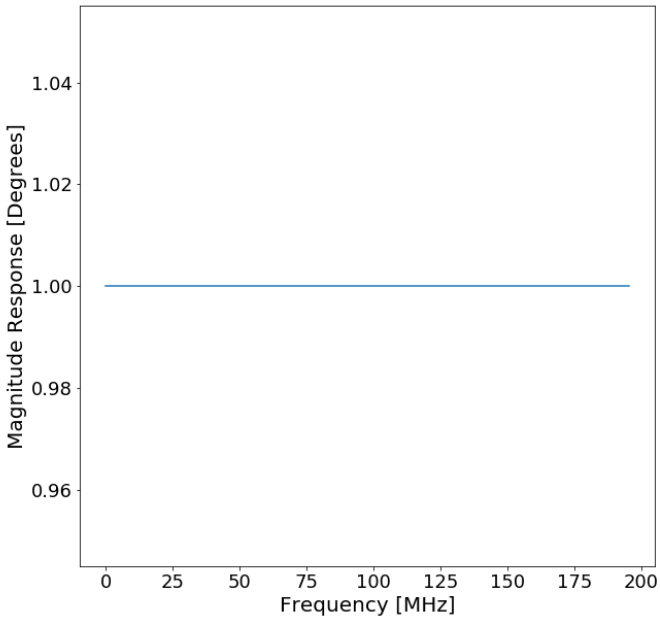

Figure 4.9: Magnitude response of the sum of the filters. It is important that the magnitude is unitary to avoid distortions.

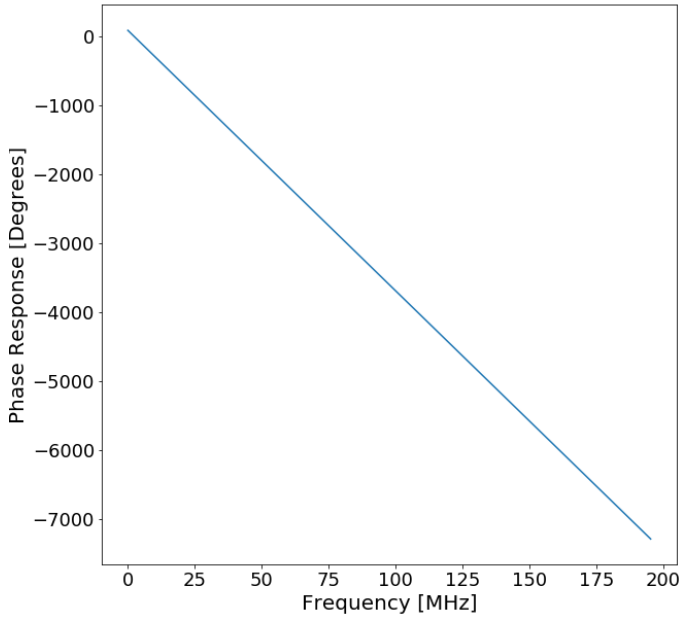

Figure 4.10: Phase response of the sum of the filters. It is important that the phase is linear with a small group delay to avoid distortions.

4.3.3 Beamforming

The last past in the MIMO SAR processing is the beamforming step. As described in chapter 3, we perform this by null-steering and canceling the signals coming from the unwanted angles. Fig. 4.11 represents this step. The unwanted signals with different pulse numbers (in red) are filtered out, along with the signal coming from the other polarization (in green), keeping the wanted signal (in blue). We reinforce the idea that which signals are 'desired' or 'unwanted' is dependent on the processing 'branch' i.e. the filter in question, alongside with the instant in time (both fast time and slow time).

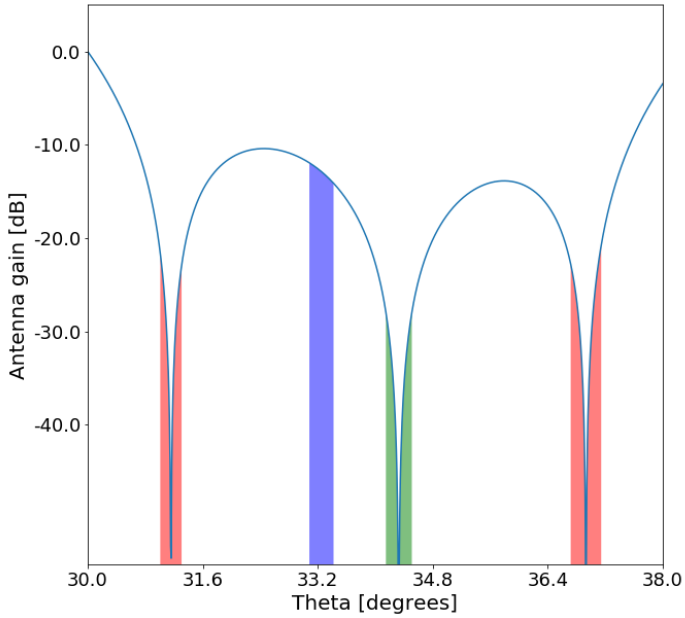

Figure 4.11: Array null-steering used for canceling unwanted returns. The blue rectangle represents the wanted signal (which is an output from a filter), the red rectangles represent signals with different pulse numbers, and the green rectangle represents the waveform from the other polarization. The blue curve represents the array factor gain. In this figure, the signal length has been changed to 500 μs to improve visibility, but the principle remains the same for $T_p = 15\,\mu s$.

4.3.4 HRWS Imaging

We now revisit the setup with the high PRF that gave poor results with classic SAR. Like before, we increase the PRF to 1.5 kHz and increase the integration time to 5.95 s. But this time we utilize of MIMO SAR processing. Figs. 4.12 and 4.13 show our results, which are very different from before. We obtain the azimuth resolution we were looking for, which is better than the original SAR situation. Likewise, the images are placed correctly in the range coordinate. This demonstrates the remarkable improvements that can be achieved using DBF on receive, which explains the intensive research activity in the past two decades to develop it.

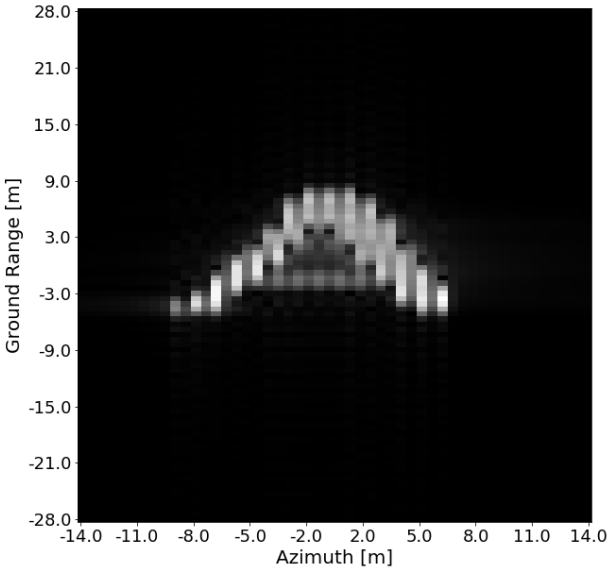

Figure 4.12: Image from the closest region of the scene generated with a PRF of 1.5 kHz. Rather than before (where the range coordinate was off and the azimuth resolution was poor), here we have a high resolution image with the correct range coordinates.

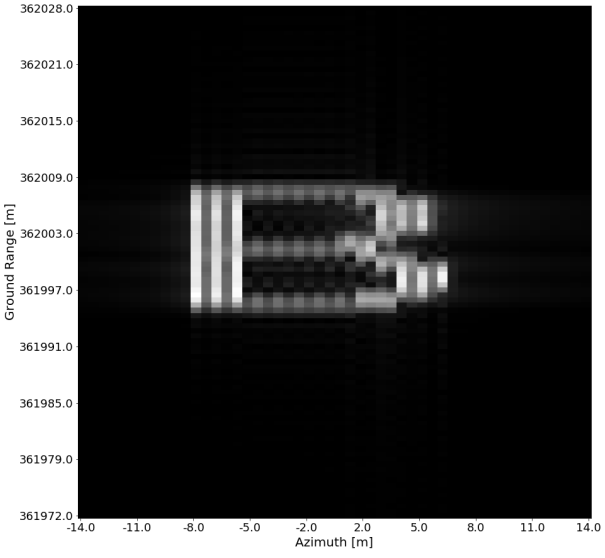

Figure 4.13: Image from the farthest region of the scene generated with a PRF of 1.5 kHz. Rather than before (where the range coordinate was off and the azimuth resolution was poor), here we have a high resolution image with the correct range coordinates. Since the resolution in the farthest region has also improved, we have achieved HRWS.

4.3.5 Polarimetric Data

One final aspect of the system remains to be tested, and that is if the system can achieve polarimetric data with two waveforms transmitted simultaneously. To test this, we split each region into two images, as in Figs. 4.14 and 4.15. The left part of each region (letters A and B) represent the first polarization, which corresponds to the up-chirp. The right part of each region (letters C and D) represent the other polarization, and the other shift-term shift-orthogonal waveform. Fig. 4.14 still represents the closest part of the imaged scene and Fig. 4.15 represents the farthest part of the imaged scene.

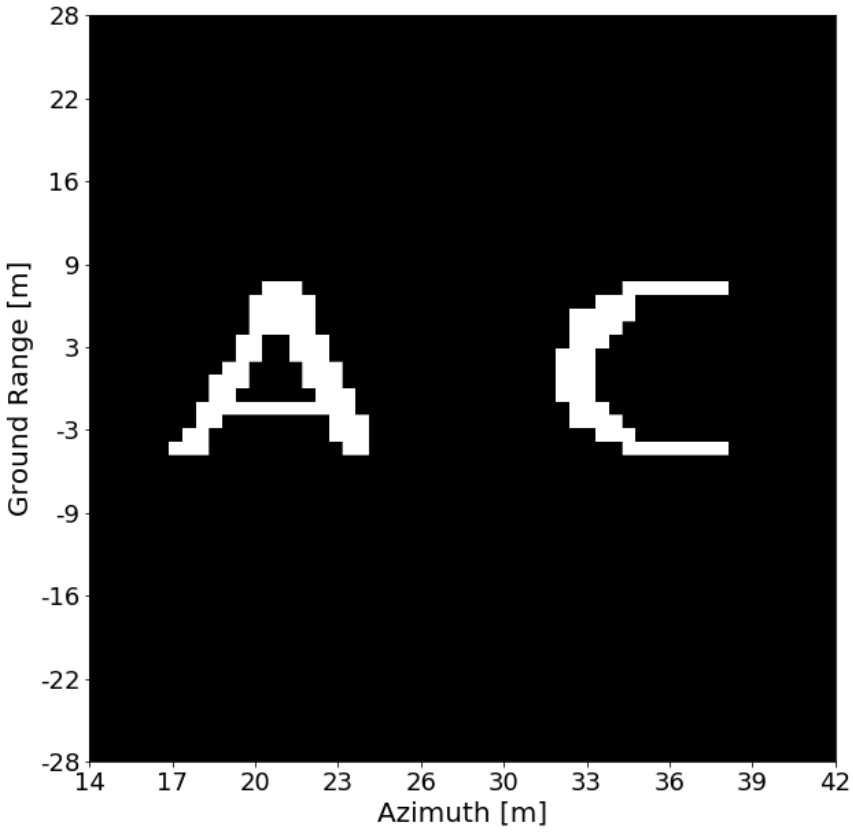

Figure 4.14: Image from the closest region of the scene. The letter A represents the reflectivity of the desired polarization, while letter C represents the reflectivity of the undesired polarization. The objective of polarimetric MIMO SAR is to suppress the returns coming from letter C.

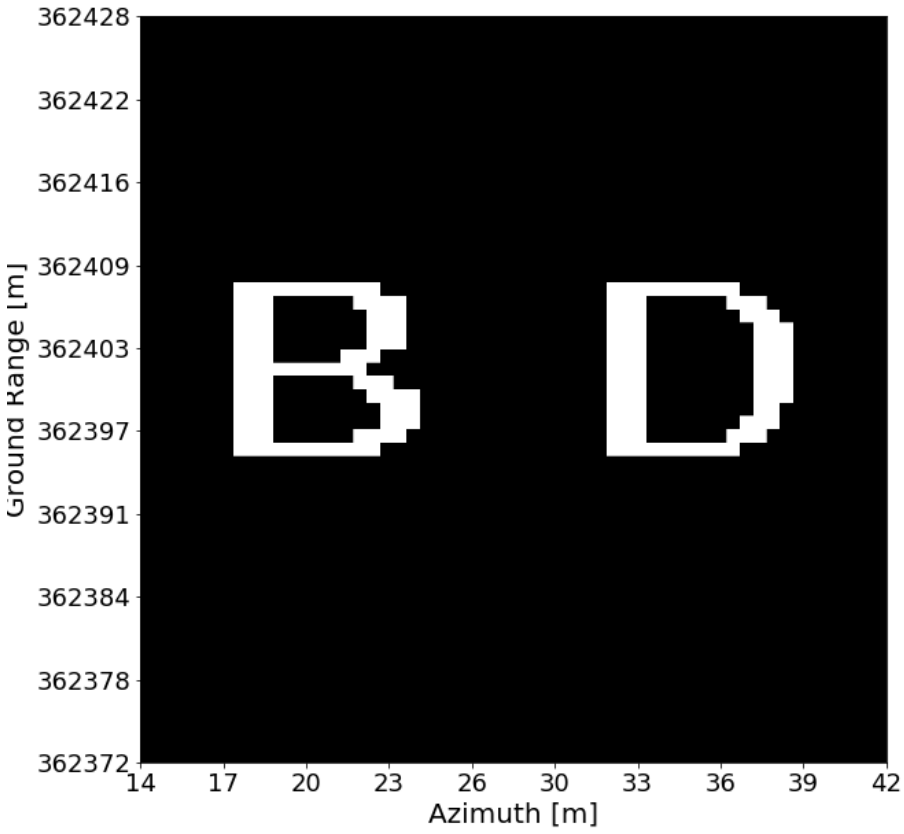

Figure 4.15: Image from the farthest region of the scene. The letter B represents the reflectivity of the desired polarization, while letter D represents the reflectivity of the undesired polarization. The objective of polarimetric MIMO SAR is to suppress the returns coming from letter D.

Figs. 4.16 to 4.19 show the result from MIMO SAR processing when the returns from the first signal are the ones desired. The first two figures are shown in a linear scale and the other two are in dB. As we can see, we filter the undesired polarization quite well, and letters C and D are almost invisible in linear scale. From an energy analysis, we obtain that the undesired polarizations are attenuated by 17.4 dB for the closest region and 19.1 dB for the farthest region. Better attenuation is reported in [35] (which reports 34 dB or higher), but that is most likely because of the LCMV beamforming used, in contrast with the simulation in this work, which implemented a simpler null-steering.

We also notice one important fact: while obtaining polarimetric information, we obtain essentially the same image we obtained before introducing another polarization. Therefore, we are able to obtain polarimetric information without compromising neither range swath nor azimuth resolution, as was predicted by the theory underlines in chapter 3. With this result, we end our MIMO SAR analysis.

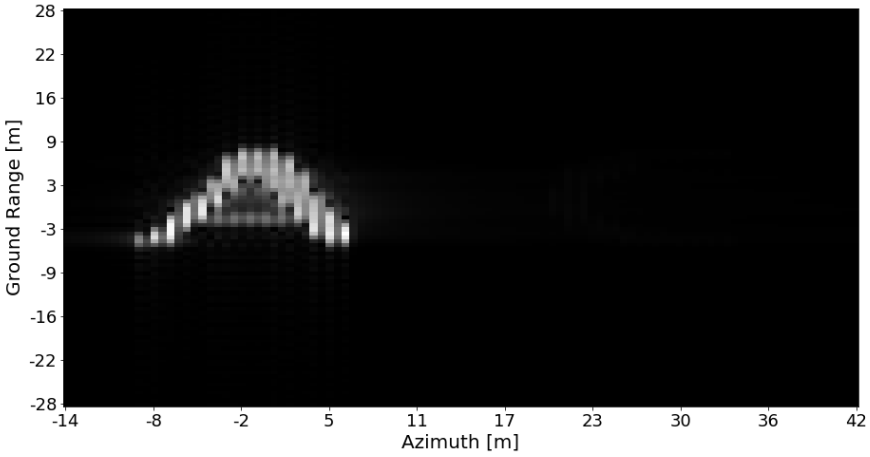

Figure 4.16: Image from the closest region of the scene. The left image (letter A) is crisp and clear, while the right image (letter C) is barely visible.

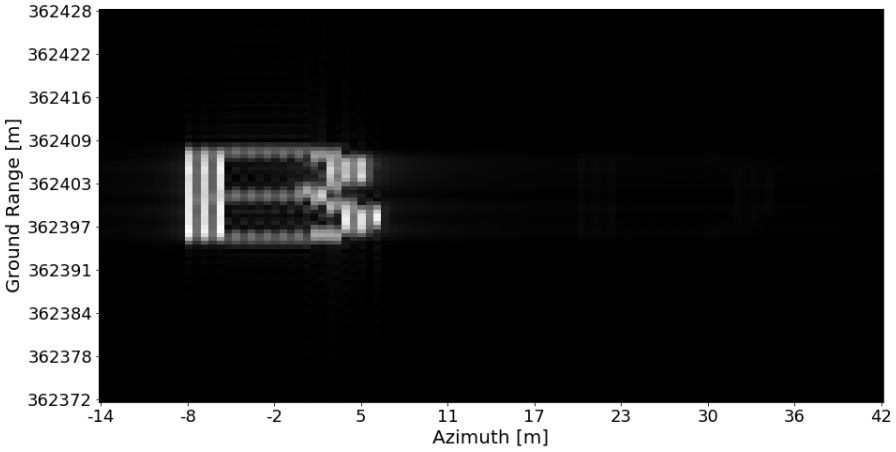

Figure 4.17: Image from the farthest region of the scene. The left image (letter B) is crisp and clear, while the right image (letter D) is barely visible.

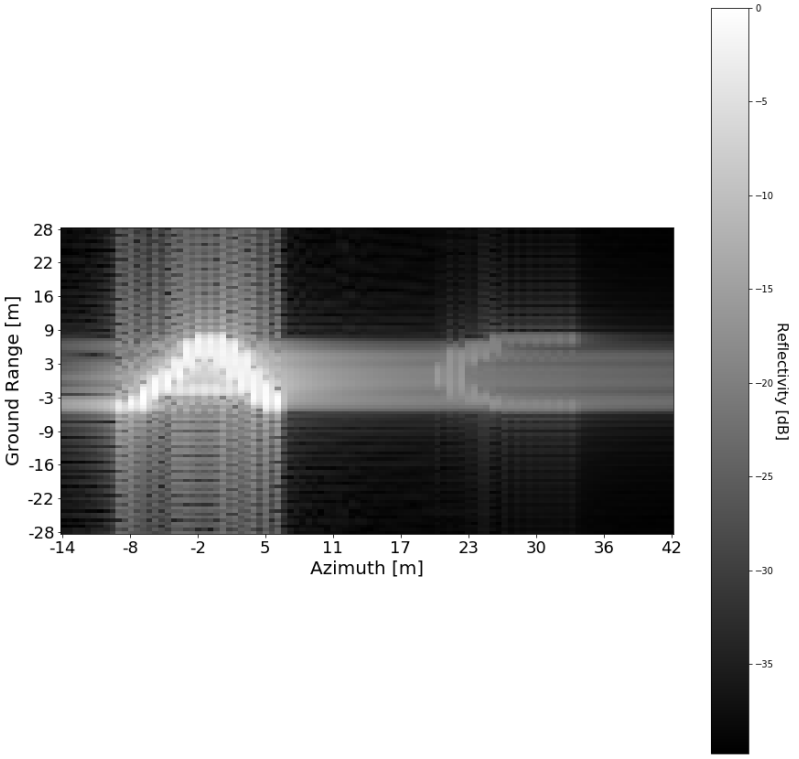

Figure 4.18: Image from the closest region of the scene in dB. The right image (letter C) is attenuated by 17.4 dB.

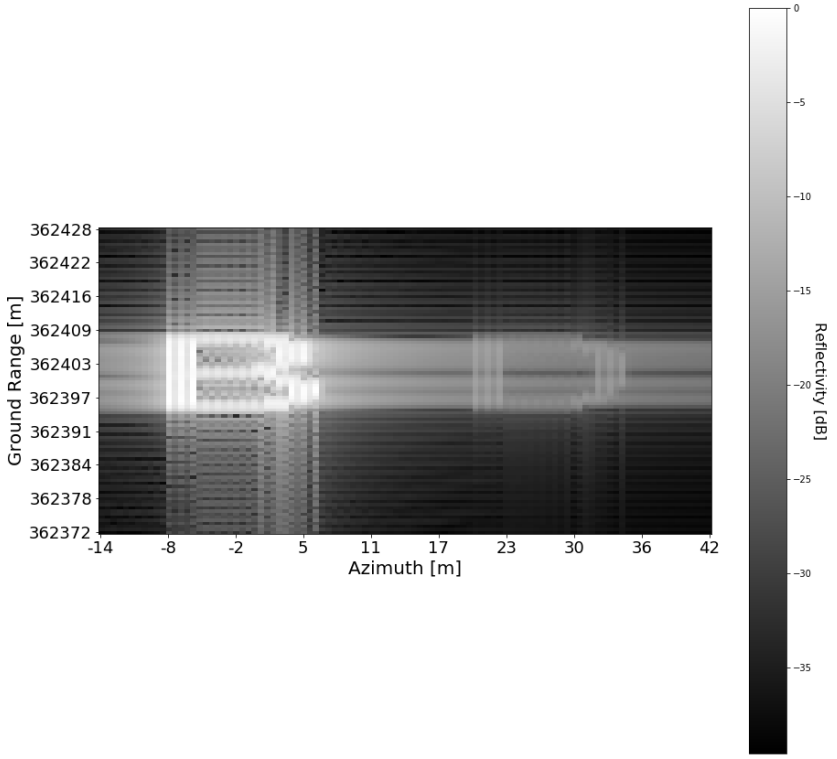

Figure 4.19: Image from the farthest region of the scene in dB. The right image (letter D) is attenuated by approximately 19.1 dB.

4.4 Conclusion

In this chapter we simulated both classic SAR and MIMO SAR systems. The classic SAR simulations showcased the intrinsic limitations of classic SAR, which seek to be remedied with MIMO SAR. When simulating a MIMO SAR system, we showcased every step of the required processing, along with examples that present the capabilities of MIMO SAR systems. From the examples shown, it should be clear that, while MIMO SAR has a cost in terms of additional processing, it presents a much more capable SAR system than traditional ones.

Chapter 5

Conclusions and Future Work

5.1 Conclusion

In this work, we have presented the new SAR technique called MIMO SAR. This technique, which employs antenna arrays on the platform and multiple transmitted waveforms, seeks to fundamentally change the limitations of SAR systems. Namely, it seeks to overcome the intrinsic trade-off between imaged area and resolution of classic SAR, and the fact that, in classic SAR, obtaining full-polarimetric information necessitates a smaller image area or a resolution deterioration.

In chapter 2, we have presented basic radar and SAR theory so as to understand where do these fundamental limitations come from. From then, we have explained in chapter 3 how MIMO SAR effectively overcomes these limitations, and the necessary hardware and processing. In chapter 4 we have shown simulations that showcase both the limitations of classic SAR and the capabilities of MIMO SAR, along with each necessary processing step.

MIMO SAR, along with DBF SAR, allow for SAR systems that provide order of magnitude improvement over classical techniques [24]. Considering the major impact that SAR has made in remote sensing, one can only imagine the benefits that these new techniques will bring to various scientific and humanitarian applications.

5.2 Future Work

For future work, we can include the development of a simulation platform that includes a more realistic model, for example one that includes aspects such as noise, antenna gain and antenna cross polarization. A simulation platform that takes into account scene height would also prove to be useful, since it changes the relationship between range and the echo direction of arrival, which was shown in chapter 3 and used in chapter 4 for the null-steering. Indeed, this change of DoA for a given range caused by scene height is a recognized problem in the literature [48].

Additionally, we also recognize that MIMO SAR literature still does not borrow many tech-

niques found on MIMO in the context of telecommunications. As an example for that, we see that the MIMO SAR system described in this work was arrived at in a somewhat intuitive fashion, with little mention of MIMO techniques that allow for the optimal separation of incoming waves. Therefore, a further integration between MIMO SAR literature and MIMO telecommunications could prove to bear fruit to better and more efficient MIMO SAR systems. Or, at least, could show a way to an optimal but computationally expensive 'ideal system', that could provide a baseline of which to compare to more practical MIMO SAR systems.

Bibliography

[1] Y. Crevier, T. Pultz, T. Lukowski, and T. Toutin, "Temporal analysis of ers-1 sar backscatter for hydrology applications," *Canadian Journal of Remote Sensing*, vol. 22, pp. 65–76, 07 2014.

[2] Åke Rosenqvist, A. Milne, R. Lucas, M. Imhoff, and C. Dobson, "A review of remote sensing technology in support of the kyoto protocol," *Environmental Science Policy*, vol. 6, no. 5, pp. 441 – 455, 2003.

[3] N. Longepe, S. Allain, L. Ferro-Famil, E. Pottier, and Y. Durand, "Snowpack characterization in mountainous regions using c-band sar data and a meteorological model," *IEEE Transactions on Geoscience and Remote Sensing*, vol. 47, pp. 406–418, Feb 2009.

[4] R. ROMEISER, "The future of sar-based oceanography: High-resolution current measurements by along-track interferometry," *Oceanography*, vol. 26, no. 2, pp. 92–99, 2013.

[5] K. C. Jezek, "Glaciological properties of the antarctic ice sheet from radarsat-1 synthetic aperture radar imagery," *Annals of Glaciology*, vol. 29, p. 286–290, 1999.

[6] C. Yun-gang, Z. Ze-zhong, N. P. L. of Geohazard Prevention, and C. P. Geoenvironment Protection, Chengdu University of Technology, "Extraction of information on geology hazard from multi-polarization sar images," No. 21(ISPRS 2008), pp. 4760–4763, Jan 2008.

[7] M. T. Fennell and R. P. Wishner, "Battlefield awareness via synergistic sar and mti exploitation," *IEEE Aerospace and Electronic Systems Magazine*, vol. 13, pp. 39–43, Feb 1998.

[8] S. Govindaraj, K. Chintamani, J. Gancet, P. Letier, B. van Lierde, Y. Nevatia, G. De Cubber, D. Serrano, M. Esbri Palomares, J. Bedkowski, C. Armbrust, J. Sanchez, A. Coelho, and I. Orbe, "The icarus project - command, control and intelligence (c2i)," in *2013 IEEE International Symposium on Safety, Security, and Rescue Robotics (SSRR)*, pp. 1–4, Oct 2013.

[9] H. McNairn and B. Brisco, "The application of c-band polarimetric sar for agriculture: a review," *Canadian Journal of Remote Sensing*, vol. 30, no. 3, pp. 525–542, 2004.

[10] U. Wegmuller, A. Wiesmann, T. Strozzi, and C. Werner, "Envisat asar in disaster management and humanitarian relief," in *IEEE International Geoscience and Remote Sensing Symposium*, vol. 4, pp. 2282–2284 vol.4, June 2002.

[11] "Analysis of sahelian vegetation dynamics using noaa-avhrr ndvi data from 1981–2003," *Journal of Arid Environments*, vol. 63, no. 3, pp. 596 – 614, 2005. Special Issue on The.

[12] D. Landgrebe, "Hyperspectral image data analysis," *IEEE Signal Processing Magazine*, vol. 19, pp. 17–28, Jan 2002.

[13] J. C. Curlander and R. N. Mcdonough, "Synthetic aperture radar: Systems and signal processing," 1991.

[14] J.-M. Martinez and T. L. Toan, "Mapping of flood dynamics and spatial distribution of vegetation in the amazon floodplain using multitemporal sar data," *Remote Sensing of Environment*, vol. 108, no. 3, pp. 209 – 223, 2007.

[15] R. Werninghaus, "TerraSAR-X mission," in *SAR Image Analysis, Modeling, and Techniques VI* (F. Posa, ed.), vol. 5236, pp. 9 – 16, International Society for Optics and Photonics, SPIE, 2004.

[16] R. Torres, P. Snoeij, D. Geudtner, D. Bibby, M. Davidson, E. Attema, P. Potin, B. Rommen, N. Floury, M. Brown, I. N. Traver, P. Deghaye, B. Duesmann, B. Rosich, N. Miranda, C. Bruno, M. L'Abbate, R. Croci, A. Pietropaolo, M. Huchler, and F. Rostan, "Gmes sentinel-1 mission," *Remote Sensing of Environment*, vol. 120, pp. 9 – 24, 2012. The Sentinel Missions - New Opportunities for Science.

[17] L. C. Morena, K. V. James, and J. Beck, "An introduction to the radarsat-2 mission," *Canadian Journal of Remote Sensing*, vol. 30, no. 3, pp. 221–234, 2004.

[18] G. Krieger, "Mimo-sar: Opportunities and pitfalls," *IEEE Transactions on Geoscience and Remote Sensing*, vol. 52, pp. 2628–2645, May 2014.

[19] J. S. Lee, K. P. Papathanassiou, I. Hajnsek, T. Mette, M. R. Grunes, T. Ainsworth, and L. Ferro-Famil, "Applying polarimetric sar interferometric data for forest classification," in *Proceedings. 2005 IEEE International Geoscience and Remote Sensing Symposium, 2005. IGARSS '05.*, vol. 7, pp. 4848–4851, July 2005.

[20] C. Liu, P. W. Vachon, and G. W. Geling, "Improved ship detection with airborne polarimetric sar data," *Canadian Journal of Remote Sensing*, vol. 31, no. 1, pp. 122–131, 2005.

[21] H. McNairn and B. Brisco, "The application of c-band polarimetric sar for agriculture: a review," *Canadian Journal of Remote Sensing*, vol. 30, no. 3, pp. 525–542, 2004.

[22] D. L. Schuler, T. L. Ainsworth, J. S. Lee, and G. D. Grandi, "Topographic mapping using polarimetric sar data," *International Journal of Remote Sensing*, vol. 19, no. 1, pp. 141–160, 1998.

[23] A. Ley, O. D'Hondt, and O. Hellwich, "Regularization and completion of tomosar point clouds in a projected height map domain," *IEEE Journal of Selected Topics in Applied Earth Observations and Remote Sensing*, pp. 1–11, 04 2018.

[24] A. Moreira, G. Krieger, I. Hajnsek, K. Papathanassiou, M. Younis, P. Lopez-Dekker, S. Huber, M. Villano, M. Pardini, M. Eineder, F. De Zan, and A. Parizzi, "Tandem-l: A highly innovative

bistatic sar mission for global observation of dynamic processes on the earth's surface," *IEEE Geoscience and Remote Sensing Magazine*, vol. 3, pp. 8–23, June 2015.

[25] F. Gini and M. Rangaswamy, *Knowledge-Based Radar Detection, Tracking, and Classification.* 10 2007.

[26] W. Carrara, W. Carrara, R. Goodman, and R. Majewski, *Spotlight Synthetic Aperture Radar: Signal Processing Algorithms.* Artech House remote sensing library, Artech House, 1995.

[27] S. J Orfanidis, *Electromagnetic Waves and Antennas.* 01 2014.

[28] Y. L. Neo, F. H. Wong, and I. G. Cumming, "Processing of azimuth-invariant bistatic sar data using the range doppler algorithm," *IEEE Transactions on Geoscience and Remote Sensing*, vol. 46, pp. 14–21, Jan 2008.

[29] C. Prati, A. M. Guarnieri, and F. Rocca, "Spot mode SAR focusing with the omega-K technique," in *IGARSS '91; Proceedings of the 11th Annual International Geoscience and Remote Sensing Symposium*, vol. 2, pp. 631–634, Jan 1991.

[30] D. Zhu, S. Ye, and Z. Zhu, "Polar format agorithm using chirp scaling for spotlight sar image formation," *IEEE Transactions on Aerospace and Electronic Systems*, vol. 44, pp. 1433–1448, Oct 2008.

[31] M. Bao, "Chirp scaling algorithm for geo sar based on fourth-order range equation," *Electronics Letters*, vol. 48, pp. 41–42(1), January 2012.

[32] A. F. Yegulalp, "Fast backprojection algorithm for synthetic aperture radar," in *Proceedings of the 1999 IEEE Radar Conference. Radar into the Next Millennium (Cat. No.99CH36249)*, pp. 60–65, April 1999.

[33] M. Schlund, F. von Poncet, D. H. Hoekman, S. Kuntz, and C. Schmullius, "Importance of bistatic sar features from tandem-x for forest mapping and monitoring," *Remote Sensing of Environment*, vol. 151, pp. 16 – 26, 2014. Special Issue on 2012 ForestSAT.

[34] G. Fornaro, F. Lombardini, A. Pauciullo, D. Reale, and F. Viviani, "Tomographic processing of interferometric sar data: Developments, applications, and future research perspectives," *IEEE Signal Processing Magazine*, vol. 31, pp. 41–50, July 2014.

[35] T. Rommel, R. Rincon, M. Younis, G. Krieger, and A. Moreira, "Implementation of a mimo sar imaging mode for nasa's next generation airborne l-band sar," in *EUSAR 2018; 12th European Conference on Synthetic Aperture Radar*, pp. 1–5, June 2018.

[36] A. S. Y. Poon, R. W. Brodersen, and D. N. C. Tse, "Degrees of freedom in multiple-antenna channels: a signal space approach," *IEEE Transactions on Information Theory*, vol. 51, pp. 523–536, Feb 2005.

[37] W. Wang, "Space–time coding mimo-ofdm sar for high-resolution imaging," *IEEE Transactions on Geoscience and Remote Sensing*, vol. 49, pp. 3094–3104, Aug 2011.

[38] W.-Q. Wang, "Virtual antenna array analysis for mimo synthetic aperture radars," *International Journal of Antennas and Propagation*, vol. 2012, 01 2012.

[39] T. Rommel, M. Younis, and G. Krieger, "Demonstration of simultaneous quad-polarization sar imaging for extended targets in mimo-sar," in *2016 German Microwave Conference (GeMiC)*, pp. 381–384, March 2016.

[40] G. Krieger, F. Almeida, S. Huber, M. Villano, M. Younis, A. Moreira, J. del Castillo Mena, M. Rodriguez-Cassola, P. Prats-Iraola, D. Petrolati, M. Suess, and N. Gebert, "Advanced l-band sar system concepts for high-resolution ultra-wide-swath sar imaging," 01 2017.

[41] G. Krieger, S. Huber, M. Villano, F. Q. d. Almeida, M. Younis, P. Lopez-Dekker, P. Prats, M. Rodriguez-Cassola, and A. Moreira, "Simo and mimo system architectures and modes for high-resolution ultra-wide-swath sar imaging," in *Proceedings of EUSAR 2016: 11th European Conference on Synthetic Aperture Radar*, pp. 1–6, June 2016.

[42] G. Krieger, N. Gebert, and A. Moreira, "Unambiguous sar signal reconstruction from nonuniform displaced phase center sampling," *IEEE Geoscience and Remote Sensing Letters*, vol. 1, pp. 260–264, Oct 2004.

[43] M. Villano, G. Krieger, and A. Moreira, "Staggered sar: High-resolution wide-swath imaging by continuous pri variation," *IEEE Transactions on Geoscience and Remote Sensing*, vol. 52, pp. 4462–4479, July 2014.

[44] M. Villano, G. Krieger, and A. Moreira, "A novel processing strategy for staggered sar," *IEEE Geoscience and Remote Sensing Letters*, vol. 11, pp. 1891–1895, Nov 2014.

[45] "Ritsar - synthetic aperture radar (sar) image processing toolbox for python." `https://github.com/dm6718/RITSAR`.

[46] H. Van Trees, *Optimum Array Processing: Part IV of Detection, Estimation, and Modulation Theory*. Detection, Estimation, and Modulation Theory, Wiley, 2004.

[47] J.-Y. Baudais, S. Meric, V. Riche, and E. Pottier, "Mimo-ofdm signal optimization for sar imaging radar," *EURASIP Journal on Advances in Signal Processing*, vol. 2016, 10 2016.

[48] G. Krieger, S. Huber, M. Villano, M. Younis, T. Rommel, P. Lopez Dekker, F. Almeida, and A. Moreira, "Cross elevation beam range ambiguity suppression (cebras) for high-resolution wide-swath and mimo-sar imaging," 07 2015.